POLITECNICO DI TORINO
Repository ISTITUZIONALE

Iteration Dependent Waveform Relaxation for Hybrid Field Nonlinear Circuit Problems

(Article begins on next page)

08 November 2022

Iteration Dependent Waveform Relaxation for Hybrid Field Nonlinear Circuit Problems

Torben Wendt, *Student Member, IEEE*, Marco De Stefano, *Student Member, IEEE*, Cheng Yang, *Member, IEEE*, Stefano Grivet-Talocia, *Fellow, IEEE*, and Christian Schuster, *Senior Member, IEEE*

Abstract—**This paper presents a novel waveform relaxation scheme to solve electromagnetically large structures loaded with lumped linear and nonlinear elements. The scheme partitions the problem into a linear electromagnetic structure and a possibly nonlinear lumped circuit, which are coupled using Thévenin interfaces across the steps of an iterative Waveform Relaxation scheme. The main novel contribution is an adaptive selection of the decoupling resistances used as port references to define incident and reflected scattering signals, whose time-domain samples are refined through iterations. The decoupling resistances are updated through iterations, with the main objective of improving convergence speed and ultimately runtime. The resulting scheme is self-adapting to terminations exploiting high dynamic range in their impedance profiles and is able to provide a suboptimal convergence rate. Three dimensional shielding structures loaded with nonlinear elements are employed as numerical examples to demonstrate the proposed method.**

Index Terms—**waveform relaxation, transients, field circuit coupling, macromodeling, nonlinear circuits**

I. INTRODUCTION

Hybrid field nonlinear circuit interactions arise in microwave and Electromagnetic Compatibility (EMC) engineering, in applications such as the design of frequency selective surfaces [1], [2], energy selective surfaces [3], waveform-dependent absorbing metasurfaces [4], [5], as well as power-dependent impedance surfaces [6]–[8]. Being nonlinear in nature, the temporal evolution for a given field excitation is of primary interest during the design of all these applications. An optimum design usually requires careful consideration of both the passive structure as well as the nonlinear loads in accordance with the electromagnetic fields and, hence, poses a complex numerical problem.

In the past, methods that have been used to solve this class of problems either directly obtain the solution by using full-wave simulation e.g. Finite-Difference Time-Domain Method (FDTD) [9], Time Domain Finite-Element Method (TDFEM) [10], Partial Element Equivalent Circuit (PEEC) [11] and Time Domain Integral Equation (TDIE) [12], or alternatively, construct a model of internal electromagnetic coupling in the structures, which is then used to find the solution for a given set of terminations and a particular excitation in a hybrid way,

T. Wendt, C. Yang, and C. Schuster are with the Institute of Electromagnetic Theory, Hamburg University of Technology, Harburger Schloßstr. 20, 21079 Hamburg, Germany (email: torben.wendt@tuhh.de, cheng.yang@tuhh.de, schuster@tuhh.de).

M. De Stefano and S. Grivet-Talocia are with the Dept. of Electronics and Telecommunications, Politecnico di Torino, C. Duca degli Abruzzi 24, 10129 Torino, Italy (email: marco.destefano@polito.it, stefano.grivet@polito.it).

e.g. by using transient convolution based techniques [13]–[17], Harmonic Balance (HB) [18], the envelope tracking method [19], or a solver of the SPICE class. Alternatively, fixed point iteration methods that solve the problem over the entire time span in each iteration can be used, such as Waveform Relaxation (WR) solvers [20]–[29] and more general Krylov subspace solvers [30]. Due to multiple evaluations to find the fixed point, these methods usually exploit models of electromagnetic coupling and terminations that are inexpensive to evaluate, which is the case for macromodels via recursive convolution and static terminations [31]–[35]. Recent publications have investigated different decoupling strategies, e.g. [36], [37], in order to decrease the number of required fixed point iterations. In general, the fastest convergence is attained under optimal impedance matching of the decoupled subsystems [38]–[40].

In this paper, the focus is on the hybrid computation of time domain responses of three dimensional, electromagnetically large, resonant, metallic structures loaded with diodes. The structures are being used for nonlinear shielding and show long lasting impulse responses and complex interactions between both nonlinear elements, passive structure, and electromagnetic fields. We first use a Method of Moments (MoM) solver to obtain the general coupling between any diode by means of a network parameters description in the form of tabulated frequency data. We then use Vector Fitting (VF) to extract macromodels from the MoM data. For computation of the transient response, we present a modified Waveform Relaxation scheme in the scattering domain. The decoupling of the terminations is achieved by Longitudinal Partitioning (LP) [21], [24], [35], where the decoupling sources are changed over iteration. When iterating between the subproblems, renormalization to adaptively chosen reference impedances takes place during the exchange of interface variables, which is again implemented in the form of recursive convolution.

We codename our proposed method as Iteration-Dependent Decoupling (IDD) as a novel extension of the standard Waveform Relaxation approaches. The main advantage of IDD is the ability to ensure convergence through iterations also in those cases in which standard WR with longitudinal partitioning fails, in particular interconnections of (almost) purely reactive electromagnetic systems with strongly nonlinear devices. In such cases, matching of both subsystems with purely resistive terminations is infeasible, so that earlier approaches [36]–[40] for tuning and optimizing WR decoupling cannot be applied.

We show that with the proposed strategy the convergence rate is influenced by the specific and adaptively tuned choice of
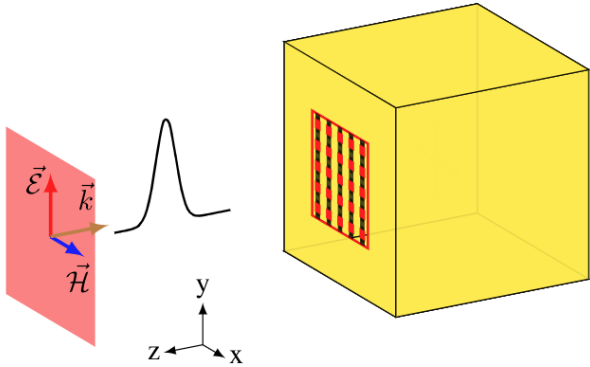
Fig. 1: A nonlinearly-loaded cavity providing an energy-selective shield from high-power incident fields. Red segments located on a regular grid throughout the aperture denote lumped ports. Figure adapted from [41].
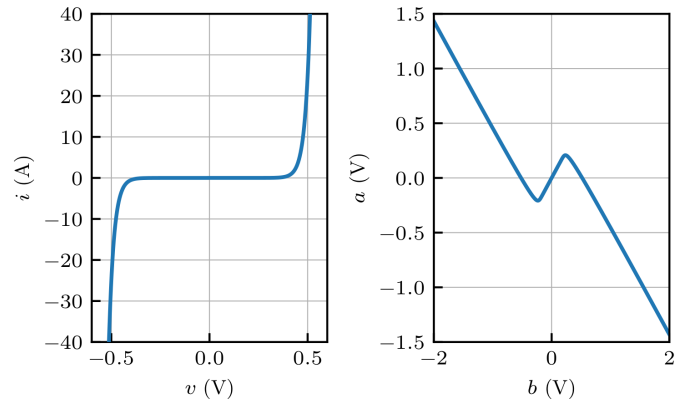

Fig. 2: Characteristic equation of an anti-parallel diode pair expressed in terms of voltage-current (left) and scattering voltage waves (right, with b incident and a reflected) referenced to $10\,\text{m}\Omega$

.

renormalization resistances, among a rich set spanning various orders of magnitude. As a result, the numerical method is intrinsically more robust than standard WR when simulating nonlinear loads. This is especially useful in a design process, during which the nonlinear loads are cycled through multiple choices and therefore the dynamic range of their impedance profiles varies widely.

The remainder of the paper is organized as follows. Section II states the problem that is addressed in this work. Section III gives a review of the longitudinal decoupling and motivates the use of iteration dependent decoupling, which is introduced in Section IV. A proof of concept example is discussed in Section V, and numerical results of the proposed method are presented in Section VI. Finally, conclusions are drawn in Section VII.

II. PROBLEM STATEMENT

We state the main problem addressed in this paper with reference to the structure depicted in Fig. 1 [42]. An electrically large electromagnetic structure, in this case a box-shaped metallic shield with an aperture, is loaded by a grid of lumped elements distributed on the aperture. These elements can be nonlinear, although particular cases with lumped linear impedances will be used to investigate convergence properties of the proposed iterative scheme. The typical scenario will use identical anti-parallel diodes at all ports, with the ports defined by the two points of contact between the terminals of the lumped termination and the linear structure, characterized by a nonlinear and purely resistive characteristic as depicted in Fig. 2. With this configuration, the shield exploits energy-selective properties, being almost transparent to low-power incident fields, with a shielding effectiveness that increases with the incident field energy [3], [43].

Our main objective is to construct an efficient and robust numerical scheme to evaluate the lumped voltages and currents at all ports, as well as to evaluate the transient electromagnetic field within the enclosure produced by an incident wave. The main difficulties in this numerical simulation problem are due to

- the electrical size of the enclosure, with a potentially large number of resonances within the modeling band;
- the possibly large number of ports;
- the presence of nonlinear terminations, which requires a time-domain approach.

As discussed in [44], once the port voltage and current signals are computed, the electromagnetic field at an arbitrary location can be efficiently evaluated through linear and fast recursive convolution operators. Therefore, this work concentrates on the calculation of the port signals.

III. BACKGROUND AND NOTATION

A. Notation

We introduce the notation adopted in this paper. Italic fonts denote scalar quantities x. Upright boldface fonts denote numeric vectors $\mathbf{x}$ (lowercase) and numeric matrices $\mathbf{X}$ (uppercase). Boldface italic fonts denote instead vector-valued signals or matrix-valued operators in time $\boldsymbol{x}(t)$ (lowercase) or frequency domain $\boldsymbol{X}(s)$ (uppercase). The identity matrix is denoted as $\mathbb{I}$.

The structure under modeling has P ports with port voltages and currents collected in vectors $\boldsymbol{v}(t)$ and $\boldsymbol{i}(t)$, respectively. Based on a set of port reference resistances collected in a diagonal matrix $\boldsymbol{R}_\mu$, we define the (voltage-normalized) scattering wave vectors as

$$\boldsymbol{a}_\mu(t) = \frac{1}{2}\left[\boldsymbol{v}(t) + \mathbf{R}_\mu\boldsymbol{i}(t)\right] \tag{1}$$

$$\boldsymbol{b}_\mu(t) = \frac{1}{2}\left[\boldsymbol{v}(t) - \mathbf{R}_\mu\boldsymbol{i}(t)\right]. \tag{2}$$

We use subscript μ to denote a specific system of port reference resistances, which will be updated through the iterations of the proposed scheme.

B. The macromodeling framework

Although several approaches for the direct time-domain solution of mixed field-circuit problems exist [9]–[12], we focus here on a well-established framework based on macromodeling. Based on the approach of [44], we first consider the

large-scale complex Linear and Time-invariant (LTI) electromagnetic system by removing its terminations. This structure can be characterized by its P-port scattering operator, either in time or frequency domain through a matrix of impulse responses or transfer functions, respectively.

Assuming an incident field excitation $e_{\text{inc}}(t)$ with Laplace transform $E_{\text{inc}}(s)$ and defining the port scattering waves $\mathbf{a}_\mu(t)$ as incident into the ports of the electromagnetic structure, we have in the Laplace domain

$$\boldsymbol{B}_\mu(s) = \boldsymbol{S}_\mu(s)\boldsymbol{A}_\mu(s) + \boldsymbol{\Theta}_\mu(s) \tag{3}$$

where vector $\boldsymbol{\Theta}_\mu(s)$ represents the contribution of the incident field to the outgoing waves at all ports under port matching conditions. In practice, this vector is a derived quantity

$$\boldsymbol{\Theta}_\mu(s) = \frac{1}{2}\left[\mathbb{I} - \boldsymbol{S}_\mu(s)\right]\boldsymbol{V}_{\text{oc}}(s) \tag{4}$$

from the open-circuit voltages at all ports excited by the incident field

$$\boldsymbol{V}_{oc}(s) = \boldsymbol{H}(s)E_{\text{inc}}(s), \tag{5}$$

where $\boldsymbol{H}(s)$ are suitable transfer functions.

We perform an initial characterization in the frequency domain. Therefore, we compute through a full wave solver (e.g. MoM) a set of $\bar{n}$ frequency samples of the scattering matrix $\boldsymbol{S}_\mu(j\omega_n)$ and transfer functions $\boldsymbol{H}(j\omega_n)$ for $n = 1, \ldots, \bar{n}$. These samples span the frequency band of interest where the spectrum of all signals to be computed is predictably confined.

Given the electrically large nature of the structure and the possibly large number of ports P, the amount of tabulated data required for a good resolution can be significant. We then construct a behavioral macromodel by fitting this data

$$\check{\boldsymbol{S}}_\mu(j\omega_n) \approx \boldsymbol{S}_\mu(j\omega_n), \quad \check{\boldsymbol{H}}(j\omega_n) \approx \boldsymbol{H}(j\omega_n) \tag{6}$$

with rational functions

$$\boldsymbol{S}_\mu(s) = \sum_{\ell=1}^L \frac{\mathbf{K}_{\mu,\ell}}{s - p_{\mu,\ell}} + \mathbf{K}_{\mu,0}, \quad \boldsymbol{H}(s) = \sum_{\ell=1}^L \frac{\boldsymbol{\Upsilon}_\ell}{s - q_\ell} + \boldsymbol{\Upsilon}_0 \tag{7}$$

where s is the complex frequency (Laplace variable), $p_{\mu,\ell}$ and q_ℓ are the model poles, here assumed to be common to all transfer function entries in order to model global resonances correctly, $\mathbf{K}_{\mu,\ell}$ and $\boldsymbol{\Upsilon}_\ell$ are the corresponding residues, and $\mathbf{K}_{\mu,0}$, $\boldsymbol{\Upsilon}_0$ capture the direct couplings. The macromodel is constructed using the well-known VF [45] in the implementation [46], which includes a suitable passivity enforcement loop, here applied to $\boldsymbol{S}_\mu(s)$ only. Finally, using standard methods [47] the model (7) is realized as a state-space form

$$\boldsymbol{S}_\mu(s) = \mathbf{C}_q(s\mathbb{I} - \mathbf{A}_q)^{-1}\mathbf{B}_q + \mathbf{D}_q \tag{8}$$

with $\mathbf{A}_q$, $\mathbf{B}_q$, $\mathbf{C}_q$, $\mathbf{D}_q$ denoting system, input, output and feedthrough matrix respectively, and converted to a SPICE netlist.

C. Macromodel-based transient analysis

The system response to a particular excitation depends on the boundary conditions impressed by the lumped elements at the ports. Placement of the lumped elements at the geometrical
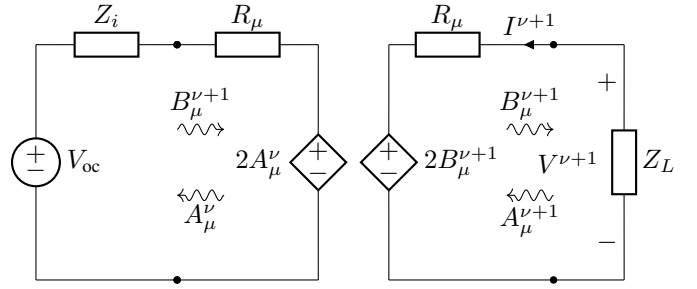

Fig. 3: Circuit interpretation of a WR iteration in the scattering domain based on a decoupling resistance R_μ, applied to a voltage divider. The left and right subcircuits are solved iteratively, using the decoupling sources $2A_\mu^\nu$ and $2B_\mu^{\nu+1}$ to update solution from one iteration to the next.

location of the ports is equivalent to attaching of lumped elements to the ports of the macromodel, which can be performed directly in a SPICE solver. Therefore, the availability of a SPICE netlist that synthesizes the non-homogeneous macromodel equations (7) provides a direct and straightforward way to perform a transient simulation under different excitation and loading conditions. This is the approach that was pursued in [44].

Here, we propose a different approach, which has the potential for more efficient numerical simulations based on a Waveform Relaxation framework. First, we cast the frequency-domain input-output relation (3) in time-domain by inverse Laplace transform, assuming vanishing initial conditions

$$\boldsymbol{b}_\mu(t) = \boldsymbol{s}_\mu(t) * \boldsymbol{a}_\mu(t) + \boldsymbol{\theta}_\mu(t) \tag{9}$$

where $*$ stands for the convolution operator and

$$\boldsymbol{\theta}_\mu(t) = \left[\mathbb{I} - \boldsymbol{s}_\mu(t)\right] * \boldsymbol{h}(t) * e_{\text{inc}}(t)/2. \tag{10}$$

Then, we discretize (9) on a uniform grid $t_m = m\delta_t$ of time samples, and we approximate the continuous convolution operators as recursive convolutions [35], denoted here by $\circledast$ and expressed as

$$\boldsymbol{\theta}_\mu(t_m) = (\mathbb{I} - \boldsymbol{s}_\mu) \circledast (\boldsymbol{h} \circledast e_{\text{inc}})(t_m)/2 \tag{11}$$

$$\boldsymbol{b}_\mu(t_m) = (\boldsymbol{s}_\mu \circledast \boldsymbol{a}_\mu)(t_m) + \boldsymbol{\theta}_\mu(t_m). \tag{12}$$

The discrete-time macromodel equations (12) are coupled with the equations of the terminations, which can be generally cast as a nonlinear operator relating voltage-current or scattering variables as

$$\boldsymbol{i}(t_m) = \mathcal{N}(\boldsymbol{v}(t_m)), \quad \text{or} \quad \boldsymbol{a}_\mu(t_m) = \mathcal{G}_\mu(\boldsymbol{b}_\mu(t_m)), \tag{13}$$

where the nonlinear map $\mathcal{G}_\mu$ provides the characteristic equations of the nonlinear loads in terms of the scattering variables. Note that the reflected waves $\boldsymbol{b}_\mu$ from the macromodel are the incident waves (inputs) for the terminations, provided that the same set of port reference resistances is used. Figure 2 provides a graphical illustration of both characteristics (13) for an anti-parallel diode termination. The approach we propose to solve these coupled equations for all time steps $m = 1, \ldots, \bar{m}$ follows the Waveform Relaxation paradigm, discussed next.

D. Basic Waveform Relaxation

The so-called Longitudinal Waveform Relaxation scheme is a simple fixed-point iteration. Instead of solving (12)-(13) for all variables at time t_m through a Newton iteration within a time-stepping outer loop (as SPICE does), a WR approach refines initial estimates of all signals through iterations $\nu = 1, 2, \ldots$. Such estimates will be denoted through superscript ν. In particular, a basic WR scheme:

1) sets $\nu = 0$ and initializes all signals at all time steps (e.g. with all-zero vectors);
2) evaluates (12) for $t_1, \ldots, t_{\bar{m}}$ with $\bar{m}$ indexing the last time sample

$$\boldsymbol{b}_\mu^{\nu+1}(t_m) = \left(\boldsymbol{s}_\mu \circledast \boldsymbol{a}_\mu^\nu\right)(t_m) + \boldsymbol{\theta}_\mu(t_m) \qquad (14)$$

(note that $\boldsymbol{\theta}_\mu(t_m)$ can be precomputed $\forall m$ during problem setup and initialization);
3) evaluates the scattering representation of the nonlinear termination (13) for all $t_1, \ldots, t_{\bar{m}}$

$$\boldsymbol{a}_\mu^{\nu+1}(t_m) = \mathcal{G}_\mu(\boldsymbol{b}_\mu^{\nu+1}(t_m)), \qquad (15)$$

4) updates iteration index $\nu \leftarrow \nu + 1$ and repeats steps 2-4 until convergence.

The above basic WR scheme is straightforward to implement but has a major drawback related to convergence. The scheme is not guaranteed to converge, and even if it converges, it may take a huge number of iterations, thus defeating the purpose of an efficient transient analysis.

E. Convergence of Basic Waveform Relaxation

We illustrate the issues related to WR convergence on a simple scalar example with linear terminations, so that a frequency-domain analysis can be performed. This is well-known material, that we report here since the results will provide useful guidelines to optimize the convergence of our proposed adaptive WR scheme.

Let us consider a simple Thévenin source with open-circuit voltage V_{oc} and internal impedance Z_i, loaded by an impedance Z_L. We choose a port reference resistance R_μ to describe both source and load through their scattering representations

$$B_\mu(j\omega) = S_\mu(j\omega)A_\mu(j\omega) + \Theta_\mu(j\omega) \qquad (16)$$
$$A_\mu(j\omega) = \Gamma_\mu(j\omega)B_\mu(j\omega) \qquad (17)$$

where

$$\Theta_\mu(j\omega) = [1 - S_\mu(j\omega)]\, V_{oc}/2. \qquad (18)$$

and

$$S_\mu(j\omega) = \frac{Z_i(j\omega) - R_\mu}{Z_i(j\omega) + R_\mu}, \quad \Gamma_\mu(j\omega) = \frac{Z_L(j\omega) - R_\mu}{Z_L(j\omega) + R_\mu}. \qquad (19)$$

Longitudinal decoupling is depicted in Fig. 3, which shows the signal estimates at iteration ν corresponding to the WR loop

$$B_\mu^{\nu+1}(j\omega) = S_\mu(j\omega)A_\mu^\nu(j\omega) + \Theta_\mu(j\omega) \qquad (20)$$
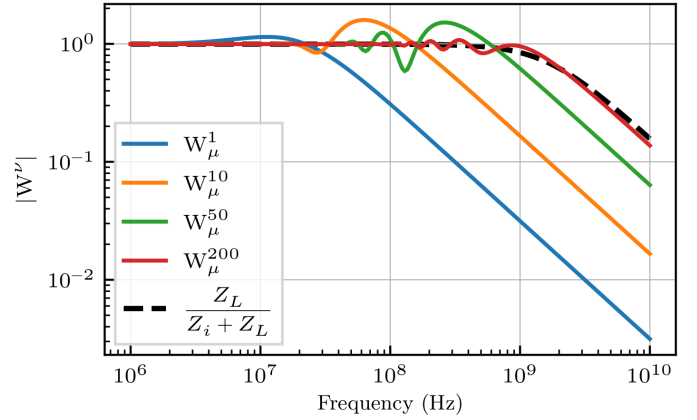$$A_\mu^{\nu+1}(j\omega) = \Gamma_\mu(j\omega)B_\mu^{\nu+1}(j\omega) \qquad (21)$$

Fig. 4: Effective transfer function W_μ^N resulting from termination of the waveform relaxation scheme after N iterations. $Z_i = R_i + j\omega L_i$ with $R_i = 50\,\Omega$ and $L_i = 1\,\mu\text{H}$; $R_\mu = 50\,\Omega$; $Z_L = 10^4\,\Omega$.

where (20) and (21) correspond to the evaluation of the subcircuits on the left and right, respectively. After a total of $\nu = 1, 2, \ldots N$ iterations we can write the load voltage (we omit arguments $j\omega$) as

$$V^N = (1 + \Gamma_\mu) \cdot \left[\sum_{\nu=0}^N (S_\mu \Gamma_\mu)^\nu\right] \cdot \frac{1 - S_\mu}{2} \cdot V_{oc} \qquad (22)$$
$$= W_\mu^N \cdot V_{oc} \qquad (23)$$

Taking the limit for $N \to \infty$ leads to the correct solution

$$\lim_{N \to \infty} W_\mu^N = (1 + \Gamma_\mu) \cdot \frac{1}{1 - S_\mu \Gamma_\mu} \cdot \frac{1 - S_\mu}{2} = \frac{Z_L}{Z_i + Z_L}. \qquad (24)$$

Convergence to the expected voltage divider holds, provided that $|S_\mu \Gamma_\mu| < 1$. Under such situation, the convergence rate is exponential, as $|S_\mu \Gamma_\mu|^\nu$. In a multiport setting, both reflection coefficients S_μ and Γ_μ become scattering matrices $\boldsymbol{S}_\mu$ and $\boldsymbol{\Gamma}_\mu$, and the convergence rate ρ_μ^ν is determined by the spectral radius $\rho_\mu = \rho(\boldsymbol{S}_\mu \boldsymbol{\Gamma}_\mu)$, which has to be $\rho_\mu < 1$.

Figure 3 depicts the effective transfer function W_μ^N after N iterations for a particular case of frequency-dependent source impedance $Z_i(j\omega) = R_i + j\omega L_i$ with $R_\mu = R_i$. The convergence speed is frequency-dependent. At low frequencies we see that $Z_i(j\omega) \approx R_\mu$, so that the source impedance is matched to the decoupling resistance. This implies that $S_\mu(j\omega) \approx 0$ and WR convergence for small ω is practically immediate. Conversely, as ω increases, both source and load impedances become significantly different from (larger than) R_μ. This mismatch causes both $S_\mu(j\omega)$ and $\Gamma_\mu(j\omega)$ to have nearly unit magnitude, implying that the series (23) converges very slowly. Even after 200 iterations the WR solution is very poor.

The above example shows that longitudinal WR schemes may be effective only when the decoupling resistance R_μ is close to either source or load effective impedances, at all frequencies. This requirement is practically impossible with a standard WR scheme for our specific problem, since:

- metallic enclosures exploit input impedances with large ranges of variations due to the presence of internal resonances. Matching such impedances with a set of

decoupling resistances may be possible only at a fixed frequency, but not over a broad band as required by our setting;

- for highly reactive structures with an input impedance $Z_i = R_i + jX_i$ such that $|X_i| \gg |R_i|$, the magnitude of the reflection coefficient (19) reads

$$|S_\mu|^2 = \frac{(R_i - R_\mu)^2 + X_i^2}{(R_i + R_\mu)^2 + X_i^2} \approx 1. \qquad (25)$$

It may be therefore impossible to match such structures with any real decoupling resistance R_μ.

- nonlinear terminations such as antiparallel diodes switch from conducting to non-conducting states during a transient simulation. The equivalent impedance profile is time-dependent. Therefore, a purely resistive matching may be performed within a given time interval, but not for a transient simulation where mutliple diode switchings occur.

In the remainder of this paper we will introduce strategies that improve the WR convergence rate, by choosing decoupling resistances as close as possible to the (suitably defined) termination resistances. The above considerations imply that a single value of R_μ is not able to provide these matching conditions, and multiple values are required.

Before proceeding, we note that the example in this section investigated the convergence of the system operator, not the convergence of the system response to a particular stimulus. If the stimulus for the given example has only low frequency content, the response reaches a high accuracy after few iterations.

IV. ITERATION DEPENDENT DECOUPLING

The proposed modification to the basic WR scheme is based on a different selection of the decoupling resistances $\boldsymbol{R}_\mu$ at different iterations, hence the term Iteration-Dependent Decoupling (IDD). The main objective is the computation of the transient port variables up to a given tolerance, and in the least number of WR iterations. The degrees of freedom to be exploited to minimize the number of iterations are provided by the (diagonal) matrix of port reference resistances, that is now assumed to be iteration-dependent and is denoted as $\boldsymbol{R}^\nu$. The selection of the best set of port resistances at each iteration is driven by the requirement of approximately matching the electromagnetic structure or its nonlinear terminations. In the linear case discussed in Section III-E, this corresponds to minimizing $|S_\mu(j\omega)|$ and $|\Gamma_\mu(j\omega)|$, respectively.

Let us consider first the requirement of matching the electro-magnetic structure. Figure 5 depicts the frequency-dependent eigenvalues of the impedance matrix of the unterminated electromagnetic shield of Fig. 1. The structure is almost completely reactive with small losses, and has several resonances within the modeling bandwidth. Therefore, these eigenvalues undergo strong variations, and a broadband matching is impossible with a single set of reference resistances.

Using large port resistance values may (approximately) match the structure at some frequencies, whereas small resistance values may achieve matching at other frequencies. A
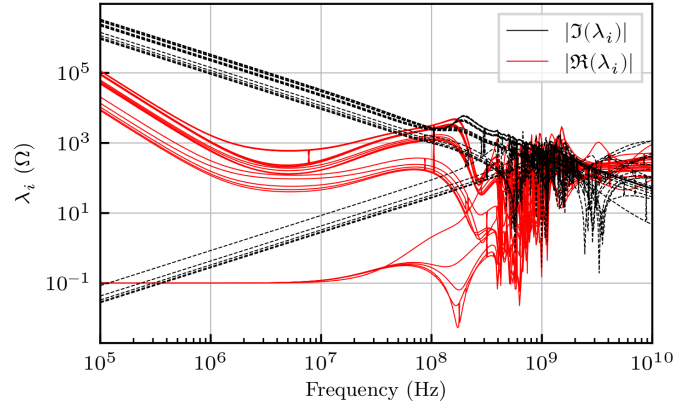

Fig. 5: Magnitude of real and imaginary part of the eigenvalues of the impedance matrix $\boldsymbol{Z}(j\omega)$ of the unterminated box of Fig. 1.

first strategy may then be to cycle the decoupling resistances between a minimum and a maximum value. This first approach is not adaptive but uses a set of predefined terminations, which can be set up by considering the span of the impedance matrix eigenvalues, as depicted in Fig. 5. We remark that approximate matching of the electromagnetic structure is viable only when the real part of the impedance (eigenvalues) is not negligible with respect to the imaginary part. For highly reactive structures, resistive matching is not a viable solution.

Full adaptivity may be introduced by pursuing the requirement of matching the nonlinear terminations. With reference to the antiparallel diodes, whose characteristics are depicted in Fig. 2, the induced transient voltages and currents at each port i may be interpreted as across a time-dependent load resistance $R_i(t)$. The latter ranges from small to large values depending on the conduction state of the diodes. Using therefore a decoupling resistance at port i equal to the observed effective (static) resistance $R_i(t_*)$ at some given time instant t_* is expected to nearly match that port in a time interval enclosing t_*, hence improving WR convergence. This consideration suggests a fully adaptive strategy that computes an estimate of voltages and currents, identifies the best decoupling resistance from these estimates, and uses this value for the next WR iteration.

Both strategies discussed above lead to a WR scheme that changes the set of decoupling resistances $\boldsymbol{R}_\mu$ at each iteration, either in a predefined way or adaptively. Throughout this work, we assume identical resistances at all ports, so that $\mathbf{R}_\mu = R_\mu \mathbb{I}$, with the values of R_μ chosen in a predefined set

$$\mathscr{R} = \{R_\mu, \ \mu \in \mathscr{I}\}, \quad \mathscr{I} = \{1, \ldots, \bar{\mu}\}. \qquad (26)$$

Elements of this set can be predetermined from the eigenvalue plot of Fig. 5 and from the nonlinear termination characteristics of Fig. 2. Adaptivity is provided by a rule $\mathcal{C}(\nu, \mathscr{I})$ that at any iteration ν selects one element from this set as

$$\mathbf{R}^\nu \xleftarrow{\mathcal{C}} R_\mu \mathbb{I}, \quad \mu \in \mathscr{I}. \qquad (27)$$

Note that $\mathcal{C}(\nu, \mathscr{I})$ is only a shorthand notation, since application of this rule may require the history of past resistance values and/or some adaptive processing of the port signals, see below.

A general pseudocode of this approach is provided in Algorithm 1 and commented below at high level. Implementation details and derivations are postponed to dedicated subsections. The proposed method consists of 1) an inner loop (lines 6–11), which evaluates only once both macromodel of the electromagnetic structure and its nonlinear terminations; 2) and an outer loop, which repeats the inner loop until numerical convergence is achieved. During an initialization step, the set (26) of reference resistances is constructed, and all corresponding scattering macromodels $S_\mu(s)$ in pole-residue form (7) are initialized (line 2). At the same time, the tabulated scattering characteristic of the nonlinear terminations are evaluated, and the source terms θ_μ are pre-computed via (11) at all time samples (line 3). The requirement of pre-computing macromodels referenced to different port resistances is discussed in Section IV-B, where details on how this conversion is performed are provided. The first set of reference resistances $\mu = 1$ is selected for the first iteration, and the wave incident on the ports of the electromagnetic structure is initialized with zero (line 4).

The first operation in the inner loop is the evaluation of the transient scattered signal from the macromodel S_μ (line 7). This operation is performed through fast recursive convolutions that return the reflected signal $b_\mu^{\nu+1}$ at all time samples. Next step (line 8) takes this signal as input to the terminations and evaluates the nonlinearly reflected signal $a_\mu^{\nu+1}$ at all time samples. This operation amounts to a simple function evaluation, as discussed in Section IV-C. Next line 9 applies the preferred selection rule for the reference resistance indexed by μ_1 to be used at next iteration, as discussed in Section IV-E. Finally, scattering signals are renormalized to this new set of resistances (lines 10–11), as shown in Section IV-A, and the loop is restarted. Iterations are stopped when estimates of the port signals of interest between two successive iterations are closer than a prescribed threshold. Since scattering signals are continuously updated and renormalized through iterations, we check convergence using the port voltages in line 12.

We should remark that the basic structure of this algorithm is the same as the standard WR with longitudinal partitioning, with the main difference in the lines 9–11 for renormalization, in addition to the required initial preprocessing (lines 1–3).

A. Renormalization of scattering signals

The proposed Iteration Dependent Decoupling (IDD) method is essentially based on a change of normalization resistances that define the port signals, which is applied at each iteration. This conversion is provided by a purely algebraic operation with negligible cost. Based on the definitions (1)-(2), we define an operator $\mathbf{T}_\mu$, mapping port voltages and currents scattering signals

$$\begin{pmatrix} a_\mu \\ b_\mu \end{pmatrix} = \underbrace{\frac{1}{2}\begin{pmatrix} \mathbb{I} & \mathbf{R}_\mu \\ \mathbb{I} & -\mathbf{R}_\mu \end{pmatrix}}_{\mathbf{T}_\mu}\begin{pmatrix} v \\ i \end{pmatrix}, \qquad (28)$$

Algorithm 1 IDD WR Implementation

Require: S_0, n, v_{oc}

1: **for** $\mu = 1$ to $\bar{\mu}$ **do**   ▷ Initialization Loop
2:     Compute S_μ, $\mathcal{G}_\mu$ ▷ Macromodels, Terminations
3:     $\theta_\mu = (v_{\mathrm{oc}} - S_\mu \circledast v_{\mathrm{oc}})/2$ ▷ Source Terms

4: $\mu_1 = 1$, $a_\mu^1 = \mathbf{0}$ ▷ Initialization
5: **for** $\nu = 1$ to N **do**   ▷ Outer Loop
6:     $\mu = \mu_1$
7:     $b_\mu^{\nu+1} = S_\mu \circledast a_\mu^\nu + \theta_\mu$ ▷ Solve macromodel
8:     $a_\mu^{\nu+1} = \mathcal{G}_\mu(b_\mu^{\nu+1})$ ▷ Solve nonlinear circuit
9:     $\mu_1 = \mathcal{C}(\nu, \mathcal{G})$ ▷ Next decoupling resistance
10:    $(v^{\nu+1}, i^{\nu+1})^{\mathrm{T}} = \mathbf{T}_\mu^{-1}(a_\mu^{\nu+1}, b_\mu^{\nu+1})^{\mathrm{T}}$
11:    $a_{\mu_1}^{\nu+1} = (v^{\nu+1} + \mathbf{R}_{\mu_1} i^{\nu+1})/2$ ▷ Renormalization
12:    **if** $\|v^{\nu+1} - v^\nu\|_\infty < \epsilon$ **then**   ▷ Break condition
13:        **return** $v^{\nu+1}$, $i^{\nu+1}$

---

and its inverse

$$\begin{pmatrix} v \\ i \end{pmatrix} = \underbrace{\begin{pmatrix} \mathbb{I} & \mathbb{I} \\ \mathbf{R}_\mu^{-1} & -\mathbf{R}_\mu^{-1} \end{pmatrix}}_{\mathbf{T}_\mu^{-1}}\begin{pmatrix} a_\mu \\ b_\mu \end{pmatrix}. \qquad (29)$$

Accordingly, renormalization from a scattering-voltage-wave representations with reference $\mathbf{R}_1$ to a new reference $\mathbf{R}_2$ is achieved by

$$\begin{pmatrix} a_2 \\ b_2 \end{pmatrix} = \mathbf{T}_2\mathbf{T}_1^{-1}\begin{pmatrix} a_1 \\ b_1 \end{pmatrix}. \qquad (30)$$

Note that in line 11 of Algorithm 1, only the upper block of (28) is applied since only the incident wave a_{μ_1} in the new normalization is required for exciting the macromodel S_{μ_1} at the next iteration.

B. Macromodel renormalization

The key for enabling fast execution in the WR loop is the availability of a set of macromodels $S_\mu(s)$ referenced to all sets of port resistances $\mathbf{R}_\mu$ that may be required at runtime. If such macromodels are available in pole-residue form (7), then the evaluation of the reflected scattering waves from the electromagnetic structure at all samples is computed in linear time through simple recursive convolution. This is only possible if the macromodel is referenced to the same set of resistances as the normalization resistance of the incident scattering wave. In this section, we discuss how to compute a pole-residue form in a different scattering representation starting from a given initial macromodel referenced to a different set of port resistances.

Let us assume an initial macromodel $S_1(s)$ in pole-residue form (7) with $\mu = 1$, which approximates the scattering responses normalized to port resistances $\mathbf{R}_1$. The corresponding state-space form is (8), with state-space matrices

$\{\mathbf{A}_1, \mathbf{B}_1, \mathbf{C}_1, \mathbf{D}_1\}$. Our objective is to determine both a state-space representation and the associated pole-residue representation following a port renormalization to a different set of resistances $\boldsymbol{R}_2$. This normalization can be written as

$$\boldsymbol{S}_2(s) = \boldsymbol{\Psi}^{-1} \left(\mathbb{I} - \boldsymbol{S}_1(s)\boldsymbol{\Phi}\right)^{-1} \left(\boldsymbol{S}_1(s) - \boldsymbol{\Phi}\right) \boldsymbol{\Psi} \qquad (31)$$

where $\boldsymbol{\Psi} = \mathrm{diag}(\psi_i)$ and $\boldsymbol{\Phi} = \mathrm{diag}(\phi_i)$, with

$$\psi_i = \frac{R_{1i} + R_{2i}}{R_{2i}}, \quad \phi_i = \frac{R_{2i} - R_{1i}}{R_{2i} + R_{1i}}. \qquad (32)$$

Understanding the first and second bracket of (31) as a system formed by two concatenated systems (see [47] for concatenation and inversion of state space system representations), which is pre- and post- multiplied by $\boldsymbol{\Psi}^{-1}$ and $\boldsymbol{\Psi}$, respectively, yields the following state-space realization for $\boldsymbol{S}_2(s)$

$$\mathbf{A}_2 = \begin{pmatrix} \mathbf{A}_1 & \mathbf{0} \\ \mathbf{B}_1\boldsymbol{\Phi}\left(\mathbb{I} - \mathbf{D}_1\boldsymbol{\Phi}\right)^{-1}\mathbf{C}_1 & \mathbf{A}_1 + \mathbf{B}_1\boldsymbol{\Phi}\left(\mathbb{I} - \mathbf{D}_1\boldsymbol{\Phi}\right)^{-1}\mathbf{C}_1 \end{pmatrix}$$

$$\mathbf{B}_2 = \begin{pmatrix} \mathbf{B}_1 \\ \mathbf{B}_1\boldsymbol{\Phi}\left(\mathbb{I} - \mathbf{D}_1\boldsymbol{\Phi}\right)^{-1}\left(\mathbf{D}_1 - \boldsymbol{\Phi}\right) \end{pmatrix} \boldsymbol{\Psi}$$

$$\mathbf{C}_2 = \boldsymbol{\Psi}^{-1} \left(\left(\mathbb{I} - \mathbf{D}_1\boldsymbol{\Phi}\right)^{-1}\mathbf{C}_1 \quad \left(\mathbb{I} - \mathbf{D}_1\boldsymbol{\Phi}\right)^{-1}\mathbf{C}_1\right)$$

$$\mathbf{D}_2 = \boldsymbol{\Psi}^{-1}\left(\mathbb{I} - \mathbf{D}_1\boldsymbol{\Phi}\right)^{-1}\left(\mathbf{D}_1 - \boldsymbol{\Phi}\right)\boldsymbol{\Psi}. \qquad (33)$$

A pole residue representation in form (7) of the renormalized state space system (33) is obtained in two steps. First, we apply a similarity transformation

$$\mathbf{S}_2(s) = \mathbf{C}_2 \left(s\mathbb{I} - \mathbf{V}\boldsymbol{\Lambda}_2\mathbf{V}^{-1}\right)^{-1} \mathbf{B}_2 + \mathbf{D}_2 \qquad (34)$$

$$= \underbrace{\mathbf{C}_2\mathbf{V}}_{\tilde{\mathbf{C}}} \left(s\mathbb{I} - \boldsymbol{\Lambda}_2\right)^{-1} \underbrace{\mathbf{V}^{-1}\mathbf{B}_2}_{\tilde{\mathbf{B}}} + \mathbf{D}_2. \qquad (35)$$

where $\boldsymbol{\Lambda}_2 = \mathbf{V}^{-1}\mathbf{A}_2\mathbf{V} = \mathrm{diag}(\lambda_\ell)$ is an eigenvalue decomposition of the state matrix and λ_ℓ are the poles of $\mathbf{S}_2(s)$. Next, the corresponding residue matrices $\mathbf{K}_{2,\ell}$ are computed using

$$\mathbf{K}_{2,\ell} = \tilde{\mathbf{C}}_{*,\ell} \cdot \tilde{\mathbf{B}}_{\ell,*} \qquad (36)$$

where $\tilde{\mathbf{C}}_{*,\ell}$ denotes the ℓ-th column of $\tilde{\mathbf{C}}$ and $\tilde{\mathbf{B}}_{\ell,*}$ denotes the ℓ-th row of $\tilde{\mathbf{B}}$, leading to

$$\boldsymbol{S}_2(s) = \sum_{\ell=1}^{\bar{L}} \frac{\mathbf{K}_{2,\ell}}{s - \lambda_\ell} + \mathbf{D}_2. \qquad (37)$$

The above renormalization produces a rational form (37) with a different structure with respect to the initial macro-model. Instead of L pole-residue pairs with associated full-rank residue matrices in (7), a total of $\bar{L}$ terms is obtained, with rank-1 residues $\mathbf{K}_{2,\ell}$. This rank reduction would be beneficial for speeding up numerical simulations based on the model; unfortunately, it is counterbalanced by a much larger number of terms $\bar{L} = 2PL$ arising from the renormalization. In turn, this makes recursive convolution approaches [35] highly inefficient in transient analysis, since the associated cost is proportional to the number of independent poles. For this reason, we have developed a dedicated fast convolution approach, which results mathematically equivalent to the approach in [35], yet dramatically more efficient for large pole and port counts.
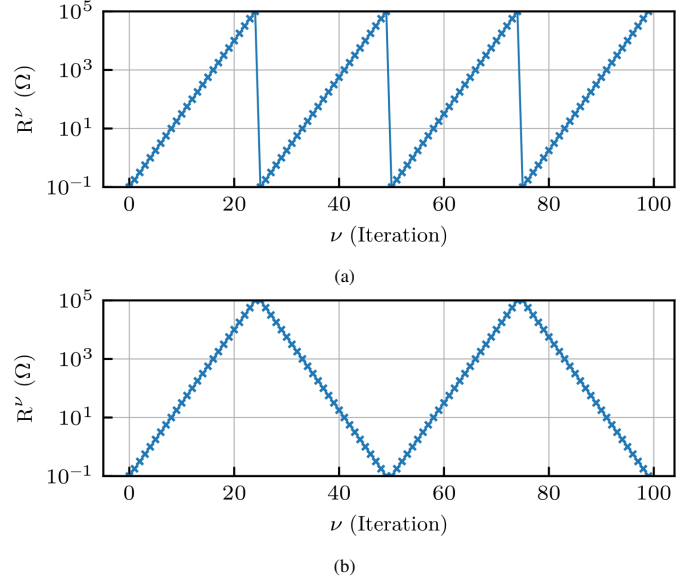

Fig. 6: Predefined selection of normalization resistances through iterations. Top: sawtooth pattern; bottom: V-cycle pattern.

C. Evaluation of nonlinear terminations

Traditional solvers of nonlinear circuits perform some form of Newton iteration at each time step to solve for the variables of interest, embedding this evaluation in an outer time-stepping loop. In a WR loop, we reverse this operation and compute the output variables resulting from the NL terminations excited by their input variables at all time steps. The nature of the investigated terminations, which may be strongly nonlinear but are purely resistive, enables this operation to be performed very efficiently, using a purely algebraic operation.

Since our WR formulation is in the scattering domain, we adopt the scattering formulation in (13) based on the operator $\mathcal{G}_\mu$, which returns at each time step t_m the reflected scattering variables $\boldsymbol{a}_\mu(t_m)$ from the corresponding incident waves $\boldsymbol{b}_\mu(t_m)$. The operator $\mathcal{G}_\mu$ is not known analytically, since the characteristic of each termination is usually known in terms of port voltages and currents. However, a fine sweep of this characteristic can be pre-computed in a preprocessing phase at given points $(\hat{V}_k, \hat{I}_k)$ in the range of interest, which are then converted to the corresponding scattering variables using (28). The result is a set of tabulated values $(\hat{B}_{\mu,k}, \hat{A}_{\mu,k})$, depicted in the right panel of Fig. 2. The evaluation of $\mathcal{G}_\mu$ during WR iteration is obtained by a simple piecewise linear or spline interpolation of such tabulated scattering-domain characteristics. Since multiple reference resistances $\boldsymbol{R}_\mu$ are used by our IDD scheme, the corresponding multiple tabulated characteristics associated to these normalization resistances are pre-computed during initialization, forming a library of representations ready to be used in runtime.

D. Predefined Iteration Dependent Decoupling

The specific choice of normalization resistances $\boldsymbol{R}^\nu$ to be used at a given iteration ν depends on the adopted rule (27). This selection may be performed according to a prescribed pattern or adaptive on the solution being computed. Here we

present two predefined patterns that provided good performance in our tests. The starting point is a set $\mathcal{R}$ of given discrete values of port resistances, see (26). Assuming that the resistances R_μ in this set for $\mu = 1, \ldots, \bar{\mu}$ are sorted in increasing order with $\bar{\mu}$ being the index of the largest resistance, we can adopt

- a *sawtooth* pattern, depicted in Fig. 6(a), which corresponds to the rule

$$\mu(\nu) \xleftarrow{\mathcal{C}} 1 + \mathrm{mod}((\nu - 1), \bar{\mu}) \qquad (38)$$

where $\mathrm{mod}(m, n)$ denotes the modulo operator (remainder of integer division of m by n);

- a *V-cycle* pattern, depicted in Fig. 6(b), which corresponds to the rule

$$\mu(\nu) \xleftarrow{\mathcal{C}} 1 + |\mathrm{mod}(\nu - 1, 2(\bar{\mu} - 1)) - (\bar{\mu} - 1)| \quad (39)$$

Of course, other patterns are possible. These two are the only ones that we tested in our numerical experiments.

E. Adaptive Iteration Dependent Decoupling

Adaptivity in the selection of the reference resistances for the next WR iteration is achieved by trying to match the nonlinear terminations, at least over a limited time span. Therefore, we define the following rule

$$R_i^\nu(t_m) = v_i^\nu(t_m) / i_i^\nu(t_m) \qquad (40)$$

where v_i^ν and i_i^ν are the port voltages and currents at the port i of interest at iteration ν, and t_m is the time instant for which the convergence rate is to be improved. Our strategy to select t_m is based on the location of the maximum difference between the voltage scattering waves available from the last two iterations normalized to the current reference.

The reference resistance to be used for next iteration is thus defined as the closest available reference resistance among the available sets

$$\mathbf{R}^{\nu+1} = \arg\min_{\mu \in \mathcal{G}} ||\mathbf{R}_\mu - \bar{R}^\nu(t_m)\mathbb{I}||, \qquad (41)$$

where $\bar{R}^\nu(t_m)$ denotes the geometric mean of $R_i^\nu(t_m)$ across the ports.

Additionally, we found that capping the maximum relative change of the reference to factors between 0.01 and 100 yields better results than unconstrained change, providing a smoother variation of the reference through iterations.

F. Linear convergence analysis

All (predefined or adaptive) implementation strategies require a detailed convergence analysis, in order to demonstrate the benefits of proposed iteration-dependent scheme. For the special case of linear terminations, a detailed frequency-domain analysis is presented in Appendix A, where an explicit expression of the WR iteration operator is derived based on a given sequence of reference resistance matrices. We report here the main conclusions.

Assuming a periodic pattern in reference resistances (with period ν_0), such as the V-cycle or the Sawtooth schemes of
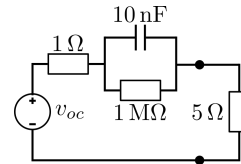

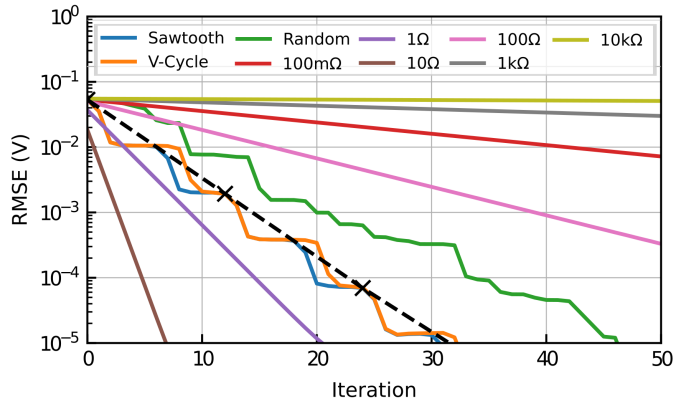Fig. 7: Example circuit of Section V-A used for Fig. 8 and Fig. 9.

Fig. 8: Instructive example of Section V-A. Deviation $\Delta v_{\mathrm{ref}}^\nu$ at each WR iteration with respect to a reference SPICE solution $v_{\mathrm{ref}}^\nu = v_{\mathrm{SPICE}}$. Solid straight lines correspond to standard WR with constant decoupling. The staircase orange line corresponds to the V-cycle IDD. Dashed black line is the proposed V-cycle plotted only at integer multiples of ν_0 (the period of the V-cycle). The green line corresponds to an aperiodic randomized selection of models. The advantage of the predefined IDD will become evident for nonlinear terminations.

Fig. 6, overall convergence is guaranteed when the spectral radius $\varrho = \rho(\boldsymbol{Q}_{\nu_0})$ of (51), repeated here for convenience,

$$\boldsymbol{Q}_{\nu_0} = \boldsymbol{M}_{\nu_0-1}\boldsymbol{M}_{\nu_0-2}\cdots\boldsymbol{M}_0 \qquad (42)$$

is less than one, where $\boldsymbol{M}_\nu$ defined as in (46). This matrix operator corresponds to a block of ν_0 iterations, each using a different decoupling resistance $\boldsymbol{R}_{\mu(\nu)}$. This should be compared to the condition for the standard WR scheme, which requires $\rho(\boldsymbol{\Gamma}_\mu \boldsymbol{S}_\mu)$ to be less than unity, where however both $\boldsymbol{\Gamma}_\mu$ and $\boldsymbol{S}_\mu$ are fixed through iterations.

Even in the general case of nonlinear terminations, the resulting convergence rate is the cumulative effect of the convergence rates associated to individual decoupling resistances. Each term contributes to speed up convergence within a given frequency interval (matching the electromagnetic structure whenever this is feasible) or a given time interval (matching nonlinear terminations), resulting in an overall benefit. This is confirmed by the numerical examples, presented next.

V. PROOF OF CONCEPT

As a proof of concept, we use a simple one port example consisting of a Thévenin equivalent formed by a voltage source v_{oc} with a series impedance Z_i. In Section V-A we illustrate the general convergence properties of the WR scheme with iteration-dependent decoupling. Section V-B shows the advantages of proposed adaptive decoupling strategy under nonlinear loading.
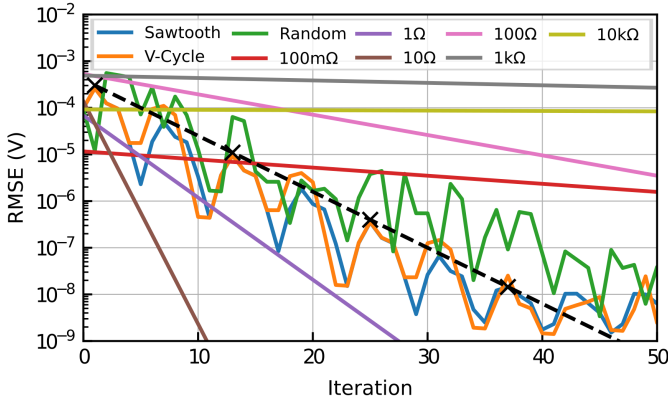
Fig. 9: As in Fig. 8, but reporting deviation $\Delta v_{\mathrm{ref}}^\nu$ between consecutive WR iteration steps, i.e., $v_{\mathrm{ref}}^\nu = v^{\nu-1}$. The dashed black line corresponds to the proposed V-cycle IDD using $v_{\mathrm{ref}}^\nu = v^{\nu-\nu_0}$.

A. Understanding the convergence pattern of the WR-IDD scheme

Let us consider a source impedance Z_i consisting of a $1\,\Omega$ resistor in series with a parallel circuit of a $10\,\mathrm{nF}$ capacitor and a $1\,\mathrm{M}\Omega$ resistor as depicted in Fig. 7. This frequency-dependent impedance has a low and high frequency limit of about $1\,\mathrm{M}\Omega$ and $1\,\Omega$, respectively. At mid frequencies (about $10\,\mathrm{kHz}$), the imaginary part is about 3 orders of magnitude larger than the real part, so that a purely resistive broadband matching is impossible. We choose a voltage source with a spectrum centered in this range, in order to emphasize these matching difficulties. In particular, we set

$$v_{\mathrm{oc}}(t) = V_0\, e^{-at^2}\cos(\omega_c t), \quad a = -\frac{\left(\frac{\omega_c}{2}b_w\right)^2}{4\cdot\log(10^{\frac{b_w}{20}})} \tag{43}$$

with $\omega_c = 2\pi\cdot 10\,\mathrm{kHz}$ and $b_w = 1$ and unit amplitude V_0.

The Thévenin source circuit is terminated with a $5\,\Omega$ resistor, and the objective is to compute the voltage across this termination. Since the reactive nature of the source impedance prevents its matching where the spectrum of the source is dominant, we concentrate on the ability of the proposed IDD scheme to match the $5\,\Omega$ termination. We choose a set of $\bar\mu = 7$ decoupling resistances $\mathcal{R} = \{100\,\mathrm{m}\Omega, 1\,\Omega, 10\,\Omega, 100\,\Omega, 1\,\mathrm{k}\Omega, 10\,\mathrm{k}\Omega, 100\,\mathrm{k}\Omega\}$, so that none of these resistances is ideally matched to the load. Lowest values of R_μ will provide better matching with respect to highest values. In a preprocessing phase, we precompute the corresponding S_μ and $\mathcal{G}_\mu$; then, we iterate in a predefined manner as depicted in Fig. 6. The computed voltage across the termination is compared to a reference signal v_{ref}^ν at iteration ν by computing the Normalized Root Mean Square Deviation (NRMSD)

$$\Delta v_{\mathrm{ref}}^\nu = \frac{\sqrt{\frac{1}{\bar m}\sum_{m=1}^{\bar m}|v^\nu(t_m) - v_{\mathrm{ref}}^\nu(t_m)|^2}}{|\max(v_{\mathrm{ref}}^\nu) - \min(v_{\mathrm{ref}}^\nu)|} \tag{44}$$

where $\bar m$ denotes the number of time samples.

Figure 8 depicts the evolution of the error (44) using as reference a signal $v_{\mathrm{ref}}^\nu = v_{\mathrm{SPICE}}$ obtained using SPICE, which we here assume to be a good approximation of the exact solution. The figure reports the results of proposed IDD

schemes as well as the results of the standard WR iterations applied with fixed decoupling resistance from the set $\mathcal{R}$. For all schemes, the error always decays through iterations. As expected, the WR scheme based on $R_\mu = 10\,\Omega$ performs best, since this value is the closest to the termination resistance. When R_μ is significantly different, convergence is very poor. Both proposed Sawtooth and V-cycle IDD provide an error decay rate that is different from one iteration to the other, as can be noted by the characteristic staircase behavior. This is also expected and is due to the different degree of matching provided by the particular reference resistance used at each iteration. The best progress towards the solution is made when using the $10\,\Omega$ decoupling resistance. A clear exponential decay is also visible when plotting the error evolution only at iterations that are multiples of the Sawtooth or V-cycle period ν_0. It can be observed that this convergence rate is a sort of "average" between the individual convergence rates that would be implied by each individual value of decoupling resistance in the set $\mathcal{R}$. It is clear that the WR-IDD is not optimal for this example, for which an optimal choice can be performed based on the value of the real and constant termination resistance. This is of course not possible in case of nonlinear termination, which is the real objective of this work. Since the Sawtooth IDD provides very similar performance of the V-cycle IDD with half a period, only the latter will be considered in the following.

Figure 9 shows the evolution of the error (44) through iterations, but using as reference the voltage estimate available from the previous iteration, $v_{\mathrm{ref}}^\nu = v^{\nu-1}$. In practical situations, a reference solution is not available, so that an error control to trigger a stopping condition can only be performed using solution estimates coming from previous iterations. This operation is straightforward when the convergence rate is uniformly exponential, as in standard WR. In proposed IDD implementations, the situation is more complicated, as discussed below.

The IDD error estimate in Fig. 9 has an oscillatory behavior, which is due to the fact that the reference for each iteration is the solution computed at a previous step, with a different normalization resistance. Since individual convergence rates associated to different decoupling resistances are different, it is expected that the accuracy gain with respect to previous iteration oscillates between large amounts (faster convergence rate) and small amounts (slower convergence rates). Therefore, the oscillation is an artefact due to an incorrect local referencing. In fact, if the reference signal is taken as $v_{\mathrm{ref}}^\nu = v^{\nu-\nu_0}$, so that the two signals used to compute $\Delta v_{\mathrm{ref}}^\nu$ in (44) are based on the same normalization resistance, the error decay is smooth and with a well-defined exponential rate.

B. Matching nonlinear terminations

We now consider a more challenging case, with a Thévenin circuit based on the same voltage source v_{oc} (amplitude $V_0 = 2.5\,\mathrm{V}$) and a purely reactive source impedance (a $1\,\mathrm{nH}$ inductance). This impedance is impossible to match since its real part is identically vanishing and the associated reflection coefficient has unit magnitude at all frequencies.
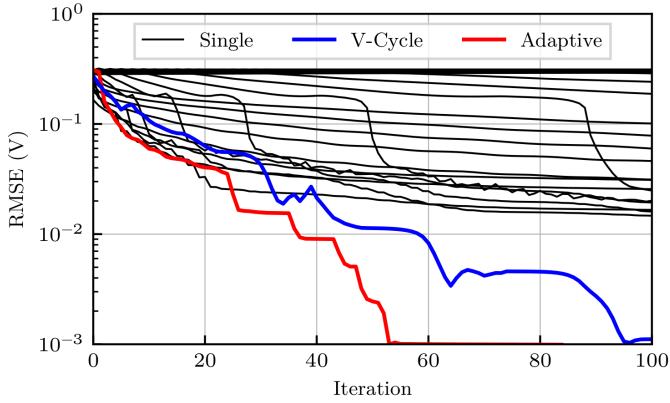
Fig. 10: Evolution of RMSE error for the example of Section V-B using standard WR decoupling with constant resistances ranging from $\{100\,\text{m}\Omega$ to $100\,\text{k}\Omega\}$ (black solid lines) and proposed IDD approaches (blue and red lines).

Fig. 12: Equivalent resistances of anti-parallel diodes at the ports of the 3×3 box excited with a $120\,\text{V}\,\text{m}^{-1}$ gaussian incident field centered at 50 MHz computed by dividing voltage by the current at each port for all time samples.
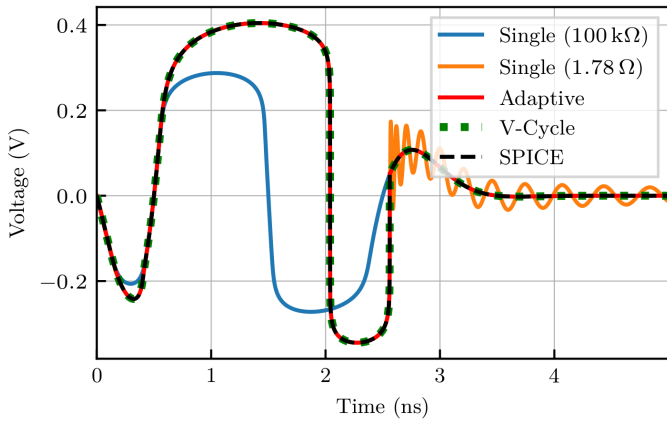

Fig. 11: Termination voltage for the example of Section V-B.

This source circuit is terminated with anti-parallel diodes, and the objective is to compute the voltage across this termination. Under these conditions, a good matching with a real constant decoupling resistance is unfeasible. Nonetheless, we show that the proposed IDD scheme provides good convergence properties.

Applying the IDD scheme, we choose the set of $\bar{\mu} = 25$ geometrically spaced decoupling resistances $\mathcal{R} = \{100\,\text{m}\Omega, ..., 100\,\text{k}\Omega\}$, we compute the corresponding S_μ and $\mathcal{G}_\mu$ and then we apply the proposed WR-IDD scheme using both predefined and adaptive implementations. Figure 10 shows the evolution over iterations of the error with respect to a reference SPICE solution, for i) a constant decoupling resistance over iteration (all values in $\mathcal{R}$) denoted by solid black lines, ii) the predefined sweep as depicted in Fig. 6(a) (V-cycle), and iii) an adaptive scheme, which chooses the next iterations decoupling resistance online as described in IV-E. The figure confirms that both predefined and adaptive approaches outperform standard WR based on any constant decoupling resistance value. The latter make a negligible progress through iterations, whereas proposed approaches converge to the reference solution. The adaptive scheme converges faster, since optimized on the solution being computed.

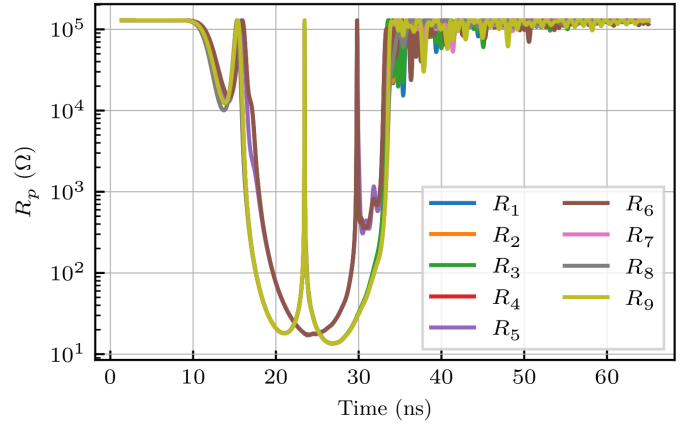An intuitive explanation can be given using Fig. 11, which

shows the obtained voltage across the anti-parallel diodes after terminating the different schemes after 120 iterations. Due to the excitation, the diodes terminating the source are driven into different conducting states over time. For the first half of the simulation interval, the diodes equivalent resistance takes values down to $500\,\text{m}\Omega$, while in the second interval, the equivalent resistance is in the range of $100\,\text{k}\Omega$. The two constant decoupling resistances ($100\,\text{k}\Omega$ in blue and $1\,\Omega$ in orange) fail to provide a good matching where the equivalent resistance is significantly different, leading to the very poor progress in the global error reduction observed in Fig. 10. Changing the decoupling resistance over iterations overcomes this limitation.

VI. SIMULATION OF NONLINEARLY LOADED ELECTROMAGNETIC SHIELDS

We now apply the proposed WD-IDD method to simulate the behavior of nonlinearly loaded (energy-selective) electromagnetic shields. We consider a box-shaped shielding structure as depicted in Fig. 1, with size $0.5m \times 0.5m \times 0.5m$. A $0.25m \times 0.25m$ aperture is present on one face of the box and is loaded with a square grid of nonlinear elements (antiparallel diodes) with a $9 = 3 \times 3$ or $25 = 5 \times 5$ arrangement. The structure is excited by a strong incident plane wave, with the electric field polarized along the Y direction, parallel to the arrangement of the diodes in each column. The waveform of this field is a modulated gaussian pulse (43) with spectrum centered at 50 MHz. In order to correctly reproduce the nonlinear effects and the generation of higher harmonics induced by the loads due to clipping, the unterminated box is characterized through broadband macromodels derived from full-wave MoM simulation data up to 1 GHz.

The goal is to compute the transient voltage across the anti-parallel diodes at the various ports of the structure. The excitation amplitude $120\,\text{V}\,\text{m}^{-1}$ of the incident electric field pulse is chosen such that the diodes switch their conduction states multiple times during the simulated time interval. In fact, the time-dependent equivalent resistance (40) derived from the computed port voltages and currents spans multiple orders of magnitude, as shown in Fig. 12.
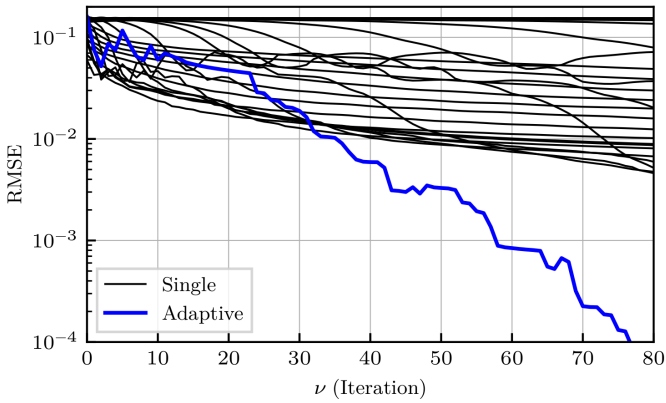
Fig. 13: Box loaded with with a 3×3 diode grid. Error with respect to a reference SPICE solution of proposed WR-IDD adaptive scheme (blue line), compared to the errors achieved by standard WR iterations based on fixed decoupling resistances ranging from $1\,\Omega$ to $100\,\mathrm{k}\Omega$ (black lines).

Fig. 15: Box loaded with with a 5×5 diode grid. Adaptive choices of the decoupling resistance performed by the WR-IDD scheme during runtime.
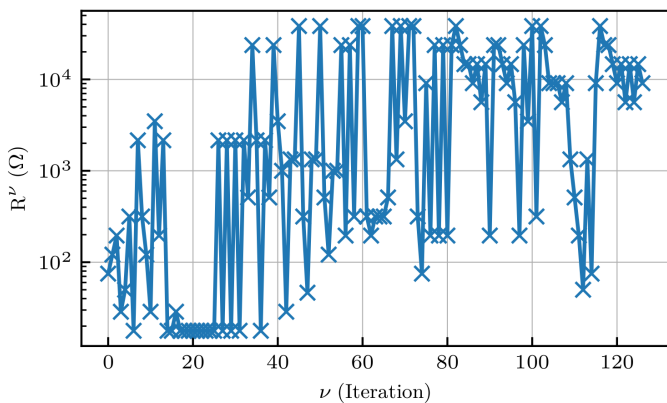

Fig. 14: Box loaded with with a 3×3 diode grid. Adaptive choices of the decoupling resistance performed by the WR-IDD scheme during runtime.

Applying the adaptive IDD scheme, we choose a set of $\bar{\mu} = 25$ geometrically spaced decoupling resistances $\mathcal{R} = \{1\,\Omega, \dots, 100\,\mathrm{k}\Omega\}$, we compute the corresponding S_μ and $\mathcal{G}_\mu$ operators, and we apply the proposed WR-IDD scheme using the adaptive implementation. Figure 13 shows the evolution over iterations of the error with respect to a reference SPICE solution, using: i) a constant decoupling resistance at all WR iterations (solid black lines, one line for each individual resistance value in $\mathcal{R}$); ii) the adaptive scheme, which chooses the decoupling resistance for the next iteration during runtime, as described in Section IV-E. The figure confirms that the adaptive approach outperforms standard WR based on any constant decoupling resistance value. The latter makes a negligible progress through iterations, whereas the proposed approach converges to the reference solution.

Except for the multiport extension, this example is similar to the one port example used as a proof of concept in Section V-B, since the box is electrically small at the frequencies excited by the incident field. In such frequency band, the input impedance of the linear electromagnetic (unterminated) structure is dominantly reactive. Very little energy dissipation is performed by the linear structure during the standard longitudinal decoupling waveform relaxation scheme. This is confirmed by the black solid curves denoting the fixed
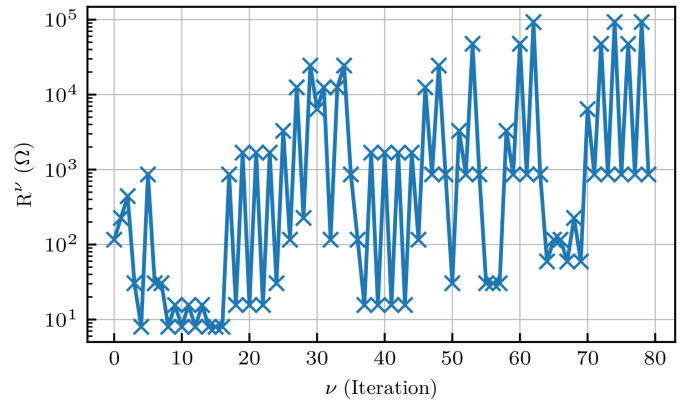
decoupling in Fig. 13, which mostly show negligible progress compared to the adaptive scheme.

Figure 14 shows the sequence of decoupling resistance values that are automatically selected by the adaptive scheme. For the first twenty iterations, the scheme chooses relatively low decoupling resistances, which can be linked to matching the diodes in their conducting state. Once the relative change over iterations becomes small enough, the scheme proceeds to attempt matching the diodes closer to the low conductance state. Also this behaviour is in line with the observations made for the one port example of Section V-B.

The above general observations are confirmed by the results obtained on a second example, namely the box loaded by a 5×5 diode grid. In this second case, we increase the incident field amplitude to $350\,\mathrm{V\,m^{-1}}$, and we apply the proposed WR-IDD adaptive scheme to evalute all port voltages and currents. Similarly to the previous 3×3 grid example, the proposed adaptive scheme updates the decoupling resistances while trying to match the diodes in their time-dependent conduction states. The results of this dynamic selection are depicted in Fig. 15.

Figure 16 shows the obtained voltage across one termination port at different iterations compared to a SPICE reference solution, for: (a) decoupling with a fixed *high resistance* ($180\,\mathrm{k}\Omega$); (b) decoupling with a fixed *intermediate resistance* ($3.3\,\mathrm{k}\Omega$); (c) decoupling with a fixed *low resistance* ($10\,\Omega$); and (d) the proposed adaptive scheme with $\bar{\mu} = 25$ geometrically spaced decoupling resistances $\mathcal{R} = \{10\,\Omega, \dots, 200\,\mathrm{k}\Omega\}$. Decoupling with a single high resistance in Fig. 16a leads to a poor performance as the decoupling fails to match the terminations at early times, where the diodes are in a conductive state due to the high-power excitation. When decoupling with a single intermediate resistance ($3.3\,\mathrm{k}\Omega$) as shown in Fig. 16b, the diodes are sufficiently matched in their conductive state, which yields a fair approximation of the system response for early time, but fails for late time where the effective resistance of the diodes in their nonconducting states is much larger. As a result, significant differences compared to SPICE remain after $\nu = 60$ iterations. Further decreasing of the decoupling resistance to $10\,\Omega$ in Fig. 16c shows that the obtained solution after 60 iterations is accurate up to only
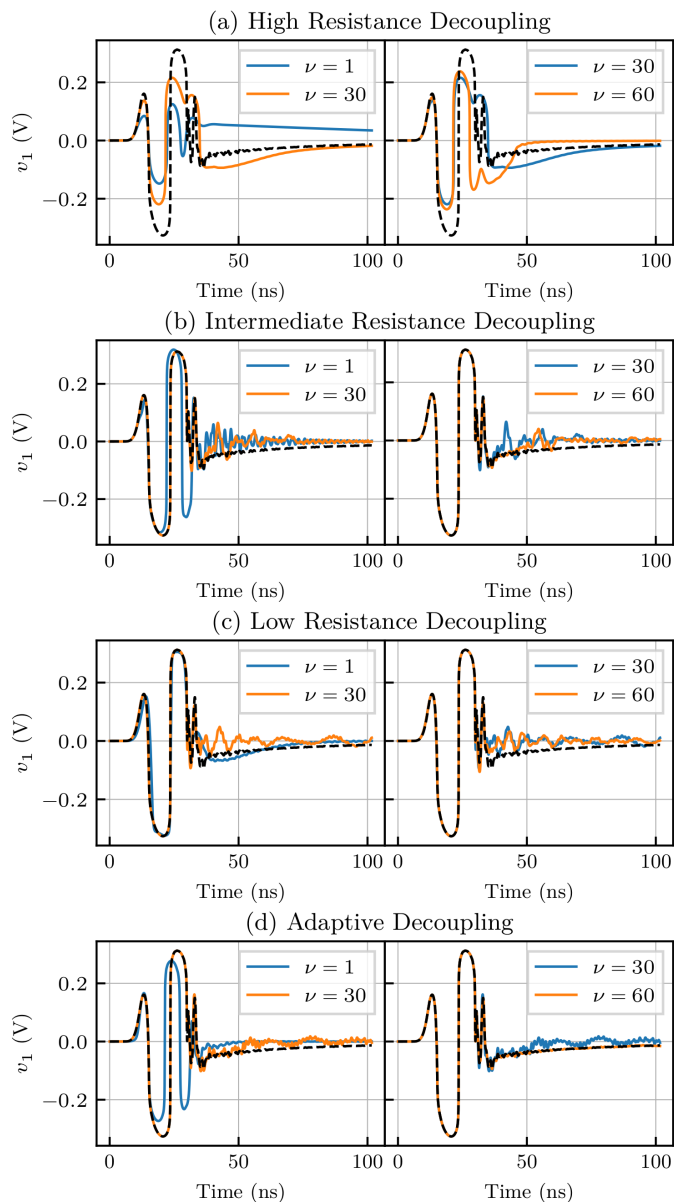
(a) High Resistance Decoupling

(b) Intermediate Resistance Decoupling

(c) Low Resistance Decoupling

(d) Adaptive Decoupling

Fig. 16: Comparison of voltages at one port of the box loaded with with a 5×5 diode grid for four different WR decoupling: (a) fixed high resistance ($180\,\text{k}\Omega$), (b) fixed intermediate resistance ($3.3\,\text{k}\Omega$), (c) fixed low resistance ($10\,\Omega$) and (d) proposed adaptive scheme.

TABLE I: Required Iterations and Computation Time

Name	Box9		Box25	
	Iter	Time	Iter	Time
SPICE [48]	-	184.35 s	-	724.69 s
WR-LPTP	501	44.74 s	600[†]	62.68 s
WR-NGMRES	9	43.7 s	19	138.38 s
Adaptive (proposed)	58	3.35 s	58	1.93 s
WR-LP				
50 Ω	291	22.83 s	600[†]	50.54 s
850 Ω	119	7.08 s	131	4.37 s

[†] denotes no convergence after 600 iterations

factor of 55× for the nine port box and 375× for the 25 port box. Additionally, the proposed adaptive approach outperforms other WR schemes as the transverse partitioning WR-LPTP [35] (mode two, three inner iterations), which does not converge within 600 iterations for the 25 port example. Furthermore, comparing to the Newton-GMRES Waveform Relaxation (WR-NGMRES [30], [34]), the proposed adaptive approach shows a speedup of 13× and 72× for the nine and 25 port examples, respectively. Finally, the standard WR-LP scheme [30] is outperformed for all 25 investigated static decoupling choices (from $100\,\text{m}\Omega$ to $10\,\text{k}\Omega$), including the best performing reported in the last line of Table I. We recall that these reference resistances are not known a priori, and that the proposed method is able to automatically select a sequence of references which leads to minimum 2× speedup.

Sweeping the excitation amplitude from $10\,\text{mV}$, $100\,\text{mV}$ to $100\,\text{V}$ peak voltage of v_{oc} gave average speedups of 175×, 55×, and 95× compared to SPICE, WR-NGMRES and WR-LPTP, respectively.

Still, there is potential for improvement, since our current implementation is single-threaded while most of the computations can be parallelized. In addition, the combination of proposed longitudinal adaptive decoupling with transverse partitioning is under way and will be documented in a future report. It is expected that the boost in efficiency achieved by this hybrid partitioning as documented in [35] will be applicable also to proposed WR-IDD scheme.

VII. CONCLUSION

This paper introduced a novel WR scheme for transient simulation of three dimensional electromagnetic structures loaded with nonlinear elements. The scheme is based on longitudinal partitioning, which separates the nonlinear terminations from the linear structure and couples them through relaxation sources that are updated through iterations until convergence. The novelty of the approach lies in adapting the relaxation sources to the terminations as the solution is being computed, based on a renormalization of the scattering port variables to suitably selected reference resistances. The latter are changed at each iteration, in order to provide heuristically optimal matching and thus speedup convergence.

The time-domain operators describing the electromagnetic structure are approximated through rational macromodels,

about $30\,\text{ns}$, which is worse than the intermediate decoupling of Fig. 16b. This can be explained by a worse mismatch compared to the intermediate decoupling at later time. In conclusion, a significant error remains after $\nu = 60$ iterations when using any prescribed constant decoupling resistance value. Figure 16d shows that the proposed method solves the observed dilemma. An accurate solution for early time is attained by first decoupling using small resistance values. As the iterations progress, the method automatically updates the decoupling resistances to larger values, leading to faster convergence in the low conductance state of the diodes.

Table I shows that the proposed adaptive method outperforms a number of alternative simulation approaches for the investigated examples. In particular, we can see that compared to the time required by the standard SPICE, we gain a speedup

whose evaluation is performed through recursive convolutions. A piecewise approximation of the nonlinear characteristics of the terminations in the scattering domain allows a direct forward evaluation, thus avoiding Newton-like iterations. The numerical results show that the proposed method can decrease the number of required iterations for nonlinear terminations compared to standard longitudinal partitioning, reducing the overall computational cost. In particular, the proposed scheme provides a fair convergence rate also in those extreme cases of highly reactive structures terminated in strongly nonlinear devices, when standard WR fails.

This work provided the general framework and a proof of concept of iteration-dependent WR decoupling. Further research is under way to optimize the heuristic rules currently used for the selection of the best decoupling scheme during runtime, and to parallelize all computational stages.

APPENDIX A
LINEAR CONVERGENCE ANALYSIS

The convergence rate of the proposed WR-IDD scheme is derived in the frequency domain assuming a P-port Thévenin source with open-circuit voltage vector $\boldsymbol{V}_{\mathrm{oc}}$ and internal impedance matrix $\boldsymbol{Z}_i$, to be decoupled from a load impedance $\boldsymbol{Z}_L$. All matrices and vectors are assumed to be frequency-dependent, and we will omit their argument $(j\omega)$.

Since scattering wave vectors are renormalized at each iteration ν, we base this convergence study on the vectors of port voltages $\boldsymbol{V}_\nu$ and currents $\boldsymbol{I}_\nu$, which are uniquely defined, and which we collect in a single block vector $\boldsymbol{X}_\nu$. Given a suitable iteration-dependent selection rule $\mu = \mu(\nu)$ for the reference resistances [we also omit argument (ν) in this derivation], each iteration of the proposed IDD scheme:

1) selects the set of resistances $\mathbf{R}_\mu$ to be used in the next step and converts the voltage-current pairs to scattering variables defined by these normalization resistances;
2) applies the linear macromodel operator (3) in its scattering form, referenced to $\mathbf{R}_\mu$;
3) computes the effect of the termination, which in the linear case is achieved through its scattering matrix referenced to $\mathbf{R}_\mu$;
4) converts the scattering vectors to voltages and currents.

A simple algebraic derivation leads to the following expression, which summarizes the above steps as

$$\boldsymbol{X}_{\nu+1} = \boldsymbol{M}_\nu \boldsymbol{X}_\nu + \boldsymbol{N}_\nu \boldsymbol{V}_{\mathrm{oc}} \qquad (45)$$

where

$$\boldsymbol{M}_\nu = \mathbf{T}_\mu^{-1} \begin{pmatrix} \boldsymbol{\Gamma}_\mu \boldsymbol{S}_\mu & \mathbf{0} \\ \boldsymbol{S}_\mu & \mathbf{0} \end{pmatrix} \mathbf{T}_\mu, \qquad (46)$$

$$\boldsymbol{N}_\nu = \frac{1}{2} \mathbf{T}_\mu^{-1} \begin{pmatrix} \boldsymbol{\Gamma}_\mu \\ \mathbb{I} \end{pmatrix} [\mathbb{I} - \boldsymbol{S}_\mu], \qquad (47)$$

with $\boldsymbol{S}_\mu$ and $\boldsymbol{\Gamma}_\mu$ denoting the scattering matrices of source and termination circuits, respectively.

Applying the recursion rule (45) for a block of $\nu + 1$ iterations and assuming $\boldsymbol{X}_0 = \mathbf{0}$ leads to

$$\boldsymbol{X}_{\nu+1} = \boldsymbol{W}_\nu \boldsymbol{V}_{\mathrm{oc}} \qquad (48)$$

where

$$\begin{aligned} \boldsymbol{W}_\nu &= \sum_{i=0}^{\nu} \left(\boldsymbol{M}_\nu \boldsymbol{M}_{\nu-1} \cdots \boldsymbol{M}_{i+1} \boldsymbol{N}_i \right) \\ &= \sum_{i=0}^{\nu} \left[\prod_{j=0}^{\nu-i-1} \boldsymbol{M}_{\nu-j} \right] \cdot \boldsymbol{N}_i \end{aligned} \qquad (49)$$

is the approximation of the transfer matrix between the voltage source vector and the port voltages and currents.

The above expression is best interpreted in the framework of proposed WR-IDD with predefined selection rules (V-cycle or Sawtooth, see Fig. 6), which correspond to a periodic function $\mu(\nu)$ with period ν_0. This implies that $\boldsymbol{M}_\nu$ is periodic with the same period, so that $\boldsymbol{M}_{\nu_0+\nu} = \boldsymbol{M}_\nu$, and similarly for $\boldsymbol{N}_\nu$. Evaluating now (48) at any integer multiple $\nu = q\nu_0$ of this period leads to the following expression

$$\boldsymbol{X}_{q\nu_0} = \boldsymbol{W}_{q\nu_0-1} \cdot \boldsymbol{V}_{\mathrm{oc}} = \sum_{i=0}^{q-1} \boldsymbol{Q}_{\nu_0}^i \cdot \boldsymbol{W}_{\nu_0-1} \cdot \boldsymbol{V}_{\mathrm{oc}} \qquad (50)$$

where

$$\boldsymbol{Q}_{\nu_0} = \boldsymbol{M}_{\nu_0-1} \boldsymbol{M}_{\nu_0-2} \cdots \boldsymbol{M}_0. \qquad (51)$$

We recognize in (50) a geometric series similar to (23), whose rate of convergence is governed by the spectral radius $\varrho := \max |\lambda_i (\boldsymbol{Q}_{\nu_0})|$ of $\boldsymbol{Q}_{\nu_0}$. This matrix is obtained as the multiplication of individual terms (46). Each of these terms has P vanishing eigenvalues and a spectral radius $\rho(\boldsymbol{\Gamma}_\mu \boldsymbol{S}_\mu)$ computed from the scattering matrices of source and termination circuits at the particular normalization $\mathbf{R}_{\mu(\nu)}$ used at iteration ν. The spectral radius of $\boldsymbol{Q}_{\nu_0}$ is thus computed on a matrix that accumulates the contribution of all individual matrix terms $\boldsymbol{M}_\nu$, evaluated over the full set of decoupling resistances in the V-cycle or Sawtooth period. The overall contractivity $\varrho < 1$ of $\boldsymbol{Q}_{\nu_0}$ is thus achieved by inheriting contractivity of the individual matrix terms.

We conclude this section by noting that the convergence of the adaptive scheme can only be assessed on a statistical basis through (48)-(49), since no clear periodic behavior is imposed. Nonetheless, the same qualitative considerations apply, and the overall convergence rate is governed by the spectral radius of the matrix product accumulated in the leading term of $\boldsymbol{W}_\nu$. Since individual terms of this product are adaptively selected to match at best the static resistance of the terminations where error is largest, there is a high probability that the adaptive scheme converges faster than any preassigned periodic sequence, even in presence of nonlinear terminations.

APPENDIX B
FAST CONVOLUTION

As discussed in Sec. IV-B, traditional recursive convolution approaches for the transient evaluation of the macromodel as in (9) or its discretized form (12) are highly inefficient when the number of poles L and ports P is large. This section presents an alternative approach that proves very efficient under these conditions. As in [35], we assume that the input time

signals are piecewise linear on the uniform grid $t_m = m\delta_t$, thus admitting the representation for the j-th component

$$a^j(t) = \sum_m \alpha_m^j \Lambda(t - t_m) \qquad (52)$$

where $\Lambda(t)$ is the unit triangle centered at $t = 0$ with semi-width δ_t. Defining the (closed-form) response of a first-order system with a single pole p_ℓ to the input signal $\Lambda(t)$ as

$$\hat{s}_\ell(t) = \mathcal{L}^{-1}\{(s - p_\ell)^{-1}\} * \Lambda(t), \qquad (53)$$

we can express the total output signal at port i of the macromodel due to a single input $\Lambda(t)$ at port j as

$$\hat{s}^{ij}(t) = \sum_{\ell=1}^{L} k_\ell^{ij} \cdot \hat{s}_\ell(t), \qquad (54)$$

where k_ℓ^{ij} denotes the ij-th entry of the residue matrix $\mathbf{K}_{\mu,\ell}$ associated to the ℓ-th pole in (7). Denoting as $\hat{\boldsymbol{s}}^{ij}$ the vector collecting the time samples of (54) for $\{t_1, \ldots, t_M\}$, and denoting the corresponding output samples at port i excited by a signal (52) at port j as $\boldsymbol{b}^{ij}$, we see that

$$\boldsymbol{b}^{ij} = \hat{\boldsymbol{s}}^{ij} \star \boldsymbol{\alpha}^j \qquad (55)$$

where $\boldsymbol{\alpha}^j$ collects all coefficients in (52) and $\star$ denotes discrete convolution. Direct evaluation of (55) is performed in $O(M \log M)$ operations through standard FFT/inverse FFT. Since the macromodel responses $\hat{\boldsymbol{s}}^{ij}$ are independent on the inputs, they can be precomputed in the setup phase, thus making the runtime cost independent on the number of poles.

As a second layer of computational cost reduction, we further perform an accuracy-controlled operator compression. We collect all samples (54) in a 3-way tensor $\hat{\mathcal{S}} \in \mathbb{R}^{M \times P \times P}$. Next, we use the Singular Value Decomposition (SVD) on the mode-1 matricization [49] of $\hat{\mathcal{S}}$ to express the full set of P^2 elementary triangle responses as a linear combination of $\rho \ll P^2$ basis functions, see [50] for details. These basis functions are convolved (using FFT/iFFT) with each input and are then mapped through the right singular values/vectors back to the original $\mathbb{R}^{M \times P}$ space, reducing the required number of convolutions from P^2 to $\rho \cdot P$. As shown in [50], this entire procedure can be accuracy-controlled by tuning the SVD truncation threshold. As an example, using a threshold 10^{-6} leads to an overall speedup of $700\times$ with respect to the standard recursive convolution [35] when applied to the 25-port box example.

REFERENCES

[1] S. Monni, D. J. Bekers, M. van Wanum, R. van Dijk, A. Neto, G. Gerini, and F. E. van Vliet, "Limiting frequency selective surfaces," in *2009 European Microwave Conference (EuMC)*, Sept 2009, pp. 606–609.

[2] S. Monni, D. J. Bekers, M. van Wanum, R. van Dijk, A. Neto, G. Gerini, and F. E. van Vliet, "Protection of RF electronics using tuneable frequency selective surfaces," in *2009 3rd European Conference on Antennas and Propagation*, March 2009, pp. 3170–3174.

[3] C. Yang, P.-G. Liu, and X.-J. Huang, "A novel method of energy selective surface for adaptive hpm/emp protection," *IEEE Antennas and Wireless Propagation Letters*, vol. 12, pp. 112–115, 2013. [Online]. Available: https://doi.org/10.1109/lawp.2013.2243105

[4] H. Wakatsuchi, D. Anzai, J. J. Rushton, F. Gao, S. Kim, and D. F. Sievenpiper, "Waveform selectivity at the same frequency," *Scientific Reports*, vol. 5, no. 1, p. 9639, 2015. [Online]. Available: https://doi.org/10.1038/srep09639

[5] G. V. Eleftheriades, "Protecting the weak from the strong," *Nature*, vol. 505, no. 7484, pp. 490–491, 2014. [Online]. Available: https://doi.org/10.1038/nature12852

[6] Z. Luo, X. Chen, J. Long, R. Quarfoth, and D. Sievenpiper, "Self-focusing of electromagnetic surface waves on a nonlinear impedance surface," *Applied Physics Letters*, vol. 106, no. 21, p. 211102, 2015. [Online]. Available: https://doi.org/10.1063/1.4921913

[7] Z. Luo, X. Chen, J. Long, R. Quarfoth, and D. Sievenpiper, "Nonlinear power-dependent impedance surface," *IEEE Transactions on Antennas and Propagation*, vol. 63, no. 4, pp. 1736–1745, 2015. [Online]. Available: https://doi.org/10.1109/tap.2015.2399513

[8] S. Kim, H. Wakatsuchi, J. J. Rushton, and D. F. Sievenpiper, "Switchable nonlinear metasurfaces for absorbing high power surface waves," *Applied Physics Letters*, vol. 108, no. 4, p. 041903, 2016. [Online]. Available: https://doi.org/10.1063/1.4940712

[9] H. Xie, J. Wang, R. Fan, and Y. Liu, "A hybrid FDTD-SPICE method for transmission lines excited by a nonuniform incident wave," *IEEE Trans. Electromagn. Compat.*, vol. 51, no. 3 PART 2, pp. 811–817, 2009.

[10] R. Wang and J. M. Jin, "Incorporation of multiport lumped networks into the hybrid time-domain finite-element analysis," *IEEE Trans. Microw. Theory Tech.*, vol. 57, no. 8, pp. 2030–2037, 2009.

[11] S. Safavi and J. Ekman, "A hybrid PEEC–SPICE method for time-domain simulation of mixed nonlinear circuits and electromagnetic problems," *IEEE Trans. Electromagn. Compat.*, vol. 56, no. 4, pp. 912–922, Aug. 2014.

[12] K. Aygun, B. Fischer, and J. Meng, "A fast hybrid field-circuit simulator for transient analysis of microwave circuits," *IEEE Trans. Microw. Theory Tech.*, vol. 52, no. 2, pp. 573–583, 2004.

[13] F. Tesche and T. Liu, "Transient response of antennas with nonlinear loads," *Electronics Letters*, vol. 11, no. 1, p. 18, 1975. [Online]. Available: https://doi.org/10.1049/el:19750014

[14] T. Liu, F. Tesche, and F. Deadrick, "Transient excitation of an antenna with a nonlinear load: Numerical and experimental results," *IEEE Transactions on Antennas and Propagation*, vol. 25, no. 4, pp. 539–542, 1977. [Online]. Available: https://doi.org/10.1109/tap.1977.1141630

[15] A. Djordjevic and T. Sarkar, "Transient analysis of electromagnetic systems with multiple lumped nonlinear loads," *IEEE Transactions on Antennas and Propagation*, vol. 33, no. 5, pp. 533–539, 1985. [Online]. Available: https://doi.org/10.1109/tap.1985.1143611

[16] K. Deiseroth and H. Singer, "Transient analysis of nonlinearly loaded arrangements consisting of thin wires and metallic patches," *Proceedings of International Symposium on Electromagnetic Compatibility*, pp. 636–641, 1995. [Online]. Available: https://doi.org/10.1109/isemc.1995.523635

[17] D. Liao, "A hybrid approach for characterizing linear and nonlinear electromagnetic scattering : Theory and applications," No. ARL-TR-6261. ARMY RESEARCH LAB, Tech. Rep. November, 2012.

[18] K. Lee, "Analysis of large nonlinearly loaded antenna arrays under multitone excitation," *Microw. Opt. Technol. Lett.*, vol. 25, no. 5, pp. 319–323, Jun. 2000.

[19] V. Subramanian and A. E. Yilmaz, "An envelope-tracking hybrid field-circuit simulator for narrowband analysis of nonlinearly loaded wire antennas," *IEEE Trans. Microw. Theory Tech.*, vol. 62, no. 2, pp. 208–223, Feb. 2014.

[20] E. Lelarasmee, A. Ruehli, and A. Sangiovanni-Vincentelli, "The waveform relaxation method for time-domain analysis of large scale integrated circuits," *IEEE Transactions on Computer-Aided Design of Integrated Circuits and Systems*, vol. 1, no. 3, pp. 131–145, 1982. [Online]. Available: https://doi.org/10.1109/tcad.1982.1270004

[21] F.-Y. Chang, "The generalized method of characteristics for waveform relaxation analysis of lossy coupled transmission lines," in *IEEE MTT-S International Microwave Symposium Digest*, - nil, p. nil. [Online]. Available: https://doi.org/10.1109/mwsym.1989.38810

[22] G. Antonini and A. E. Ruehli, "Waveform relaxation time domain solver for subsystem arrays," *IEEE Transactions on Advanced Packaging*, vol. 33, no. 4, pp. 760–768, 2010. [Online]. Available: https://doi.org/10.1109/tadvp.2010.2061229

[23] W. Beyene, "Applications of multilinear and waveform relaxation methods for efficient simulation of interconnect-dominated nonlinear networks," *IEEE Transactions on Advanced Packaging*, vol. 31, no. 3, pp. 637–648, 2008. [Online]. Available: https://doi.org/10.1109/tadvp.2008.927822

[24] M. Gander, M. Al-Khaleel, and A. Ruehli, "Waveform relaxation technique for longitudinal partitioning of transmission lines," in *2006 IEEE Electrical Performane of Electronic Packaging*, 10 2006, p. nil. [Online]. Available: https://doi.org/10.1109/epep.2006.321230

15

[25] G. Gristede, A. Ruehli, and C. Zukowski, "Convergence properties of waveform relaxation circuit simulation methods," *IEEE Transactions on Circuits and Systems I: Fundamental Theory and Applications*, vol. 45, no. 7, pp. 726–738, 1998. [Online]. Available: https://doi.org/10.1109/81.703839

[26] G. Gristede, C. Zukowski, and A. Ruehli, "Measuring error propagation in waveform relaxation algorithms," *IEEE Transactions on Circuits and Systems I: Fundamental Theory and Applications*, vol. 46, no. 3, pp. 337–348, 1999. [Online]. Available: https://doi.org/10.1109/81.751307

[27] A. R. Sridhar, N. M. Nakhla, R. Achar, M. S. Nakhla, and A. E. Ruehli, "Fast emi analysis via transverse partitioning and waveform relaxation," *IEEE Transactions on Electromagnetic Compatibility*, vol. 51, no. 2, pp. 358–371, 2009. [Online]. Available: https://doi.org/10.1109/temc.2008.2005827

[28] N. Nakhla, A. E. Ruehli, M. S. Nakhla, R. Achar, and C. Chen, "Waveform relaxation techniques for simulation of coupled interconnects with frequency-dependent parameters," *IEEE Transactions on Advanced Packaging*, vol. 30, no. 2, pp. 257–269, 2007. [Online]. Available: https://doi.org/10.1109/tadvp.2007.896010

[29] N. Nakhla, A. Ruehli, M. Nakhla, and R. Achar, "Simulation of coupled interconnects using waveform relaxation and transverse partitioning," *IEEE Transactions on Advanced Packaging*, vol. 29, no. 1, pp. 78–87, 2006. [Online]. Available: https://doi.org/10.1109/tadvp.2005.862656

[30] S. B. Olivadese and S. Grivet-Talocia, "Transient analysis of high-speed channels via newton-gmres waveform relaxation," in *2012 IEEE 21st Conference on Electrical Performance of Electronic Packaging and Systems*, 10 2012, p. nil. [Online]. Available: https://doi.org/10.1109/epeps.2012.6457886

[31] S. Grivet-Talocia, "Delay-based macromodels for long interconnects via time-frequency decompositions," *2006 IEEE Electrical Performane of Electronic Packaging*, 2006. [Online]. Available: https://doi.org/10.1109/epep.2006.321228

[32] H. Hu and S. Grivet-Talocia, "A preconditioned waveform relaxation solver for signal integrity analysis of high-speed channels," *International Symposium on Electromagnetic Compatibility - EMC EUROPE*, 2012. [Online]. Available: https://doi.org/10.1109/emceurope.2012.6396870

[33] S. Grivet-Talocia and V. Loggia, "Fast channel simulation via waveform over-relaxation," *2011 IEEE 15th Workshop on Signal Propagation on Interconnects (SPI)*, 2011. [Online]. Available: https://doi.org/10.1109/spi.2011.5898850

[34] S. B. Olivadese, S. Grivet-Talocia, C. Siviero, and D. Kaller, "Macromodel-based iterative solvers for simulation of high-speed links with nonlinear terminations," *IEEE Transactions on Components, Packaging and Manufacturing Technology*, vol. 4, no. 11, pp. 1847–1861, 2014. [Online]. Available: https://doi.org/10.1109/tcpmt.2014.2359982

[35] V. Loggia, S. Grivet-Talocia, and H. Hu, "Transient simulation of complex high-speed channels via waveform relaxation," *IEEE Transactions on Components, Packaging and Manufacturing Technology*, vol. 1, no. 11, pp. 1823–1838, 2011. [Online]. Available: https://doi.org/10.1109/tcpmt.2011.2167146

[36] T. Menkad and A. Dounavis, "Resistive coupling-based waveform relaxation algorithm for analysis of interconnect circuits," *IEEE Transactions on Circuits and Systems I: Regular Papers*, vol. 64, no. 7, pp. 1877–1890, 2017. [Online]. Available: https://doi.org/10.1109/tcsi.2017.2665973

[37] T. Menkad and A. Dounavis, "Using strictly dissipative impedance coupling in the waveform relaxation method for the analysis of interconnect circuits," *IEEE Transactions on Circuits and Systems I: Regular Papers*, vol. 68, no. 3, pp. 1283–1296, 2021.

[38] M. Gander and A. Ruehli, "Optimized waveform relaxation methods for rc type circuits," *IEEE Transactions on Circuits and Systems I: Regular Papers*, vol. 51, no. 4, pp. 755–768, 2004. [Online]. Available: https://doi.org/10.1109/tcsi.2004.826193

[39] M. J. Gander and A. E. Ruehli, "Optimized waveform relaxation solution of electromagnetic and circuit problems," in *19th Topical Meeting on Electrical Performance of Electronic Packaging and Systems*, 10 2010, p. nil. [Online]. Available: https://doi.org/10.1109/epeps.2010.5642545

[40] S.-L. Wu and M. Al-Khaleel, "Parameter optimization in waveform relaxation for fractional-order rc circuits," *IEEE Transactions on Circuits and Systems I: Regular Papers*, vol. 64, no. 7, pp. 1781–1790, 2017. [Online]. Available: https://doi.org/10.1109/tcsi.2017.2682119

[41] C. Yang, T. Wendt, M. D. Stefano, M. Kopf, C. Becker, S. Grivet-Talocia, and C. Schuster, "Analysis and optimization of nonlinear diode grids for shielding of enclosures with apertures," *IEEE Transactions on Electromagnetic Compatibility*, vol. 63, no. 6, pp. 1884–1895, 2021. [Online]. Available: https://doi.org/10.1109/temc.2021.3073106

[42] C. Yang, H.-D. Brüns, P. Liu, and C. Schuster, "Impulse response optimization of band-limited frequency data for hybrid field-circuit simulation of large-scale energy-selective diode grids," *IEEE Transactions on Electromagnetic Compatibility*, vol. 58, no. 4, pp. 1072–1080, 2016. [Online]. Available: https://doi.org/10.1109/temc.2016.2540921

[43] C. Yang, P. Liu, H.-D. Brüns, and C. Schuster, "Design aspects for HIRF protection of a rectangular metallic cavity using energy selective diode grids," in *2016 Asia-Pacific International Symposium on Electromagnetic Compatibility (APEMC)*, 5 2016. [Online]. Available: https://doi.org/10.1109/apemc.2016.7522736

[44] T. Wendt, C. Yang, H. D. Brüns, S. Grivet-Talocia, and C. Schuster, "A macromodeling-based hybrid method for the computation of transient electromagnetic fields scattered by nonlinearly loaded metal structures," *IEEE Transactions on Electromagnetic Compatibility*, vol. 62, no. 4, pp. 1098–1110, 2020.

[45] B. Gustavsen and A. Semlyen, "Rational approximation of frequency domain responses by vector fitting," *IEEE Transactions on Power Delivery*, vol. 14, no. 3, pp. 1052–1061, 1999. [Online]. Available: https://doi.org/10.1109/61.772353

[46] "Official website of idemworks," http://www.idemworks.com/, 2019.

[47] S. Grivet-Talocia and B. Gustavsen, *Passive Macromodeling*. John Wiley & Sons, Inc, 2015. [Online]. Available: https://doi.org/10.1002/9781119140931

[48] S. N. Laboratories, "Xyce analog circuit simulator," https://xyce.sandia.gov, 2019.

[49] T. G. Kolda and B. W. Bader, "Tensor decompositions and applications," *SIAM Review*, vol. 51, no. 3, pp. 455–500, 2009. [Online]. Available: https://doi.org/10.1137/07070111x

[50] S. B. Olivadese and S. Grivet-Talocia, "Compressed passive macromodeling," *IEEE Transactions on Components, Packaging and Manufacturing Technology*, vol. 2, no. 8, pp. 1378–1388, 2012. [Online]. Available: https://doi.org/10.1109/tcpmt.2012.2199320

Torben Wendt Torben Wendt (S'17) received his B.S. and M.S. degree in electrical engineering from the Technical University Hamburg (TUHH), Hamburg, Germany, in 2014 and 2017, respectively. Currently, he is working towards the Ph.D. degree at the Institute of Electromagnetic Theory, TUHH. He was a visiting researcher at the Politecnico di Torino. His current research interests include the modeling and simulation of nonlinear field circuit coupling in shielding, as well as in signal and power integrity applications.

Marco De Stefano received the M.Sc. degree in mechatronic engineering from Politecnico di Torino, Turin, Italy, in 2018, where he is currently pursuing the Ph.D. degree in electrical, electronics and communication engineering. His research interests include model-order reduction, with emphasis on parameterized macromodeling, and fast simulation methods for signal and power integrity. Mr. De Stefano was a co-recipient of the 2018 Best Paper Award of the IEEE INTERNATIONAL SYMPOSIUM ON ELECTROMAGNETIC COMPATIBILITY and the 2019 Best Student Paper of the IEEE WORKSHOP ON SIGNAL AND POWER INTEGRITY.
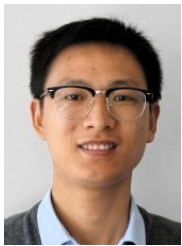
Cheng Yang (M'17) received his B.S. degree in electronic science and technology from Wuhan University (WHU), Wuhan, China, in 2009, the M.S. degree and the Ph.D. Degree with electromagnetic field and microwave technology from the National University of Defense Technology (NUDT), Changsha, China, in 2012 and 2016.

Since 2019 he has been a senior engineer of the Institut für Theoretische Elektrotechnik, Technische Universität Hamburg (TUHH), Hamburg, Germany. From 2013 to 2015, he was funded by the Chinese Scholarship Council (CSC) as a joint-PhD student at TUHH. From 2017 to 2019, he was a Faculty Member of the State Key Laboratory of Millimeter Wave at Southeast University (SEU), Nanjing, China. His current research interests include computational electromagnetics, microwave measurement techniques, electromagnetic compatibility and biology electromagnetics.

Christian Schuster (S'98 - M'00 - SM'05) received the Diploma degree in physics from the University of Konstanz, Germany, in 1996, and the Ph. D. degree in electrical engineering from the Swiss Federal Institute of Technology (ETH), Zurich, Switzerland, in 2000. Since 2006 he is full professor and head of the Institute of Electromagnetic Theory at the Hamburg University of Technology (TUHH), Germany. Prior to that he was with the IBM T. J. Watson Research Center, Yorktown Heights, NY, where he was involved in high-speed optoelectronic package and backplane interconnect modeling and signal integrity design for new server generations. His currents interests include signal and power integrity of digital systems, multiport measurement and calibration techniques, and development of electromagnetic simulation methods for communication electronics.

Dr. Schuster received IEEE Transactions on EMC Best Paper Awards in 2001 and 2015, IEEE Transactions on CPMT Best Paper Awards in 2012 and 2016, IEC DesignCon Paper Awards in 2005, 2006, 2010, 2017 and 2018, three IBM Research Division Awards between 2003 and 2005, and IBM Faculty Awards in 2009 and 2010. Also, in 2019 he received the Sustained Service to the EMC Society Award. He is a member of the German Physical Society (DPG) and several technical program committees of international conferences on signal and power integrity, and electromagnetic compatibility. He was serving as a Distinguished Lecturer for the IEEE EMC Society in the period 2012-2013, as the Chair of the German IEEE EMC Chapter in the period 2016-2019 and is currently an Associate Editor for the IEEE Transactions on EMC and a member of the Board of Directors of the EMC Society.

Stefano Grivet-Talocia (M'98–SM'07–F'18) received the Laurea and Ph.D. degrees in electronic engineering from the Politecnico di Torino, Turin, Italy.

From 1994 to 1996, he was with the NASA/Goddard Space Flight Center, Greenbelt, MD, USA. He is currently a Full Professor of electrical engineering with the Politecnico di Torino. He co-founded the academic spinoff company IdemWorks in 2007, serving as the President until its acquisition by CST in 2016. He has authored over 150 journal and conference papers. His current research interests include passive macromodeling of lumped and distributed interconnect structures, model-order reduction, modeling and simulation of fields, circuits, and their interaction, wavelets, time-frequency transforms, and their applications.

Dr. Grivet-Talocia was a co-recipient of the 2007 Best Paper Award of the IEEE TRANSACTIONS ON ADVANCED PACKAGING. He received the IBM Shared University Research Award in 2007, 2008, and 2009. He was an Associate Editor of the IEEE TRANSACTIONS ON ELECTROMAGNETIC COMPATIBILITY from 1999 to 2001 and He is currently serving as Associate Editor for the IEEE TRANSACTIONS ON COMPONENTS, PACKAGING AND MANUFACTURING TECHNOLOGY. He was the General Chair of the 20th and 21st IEEE Workshops on Signal and Power Integrity (SPI2016 and SPI2017).